Mon. Not. R. Astron. Soc. **000**, 000–000 (0000) Printed 22 January 2022 (MN LATEX style file v2.2)

Deep imaging of Fanaroff-Riley Class I radio galaxies with lobes

R.A. Laing ⋆[1], D. Guidetti[1,2], A.H. Bridle[3], P. Parma[2], M. Bondi[2]
[1] *European Southern Observatory, Karl-Schwarzschild-Straße 2, D-85748 Garching-bei-München, Germany*
[2] *INAF - Istituto di Radioastronomia, Via Gobetti 101, I–40129 Bologna, Italy*
[3] *National Radio Astronomy Observatory, 520 Edgemont Road, Charlottesville, VA 22903-2475, U.S.A.*

Received

ABSTRACT

We present deep, high-resolution imaging of the nearby Fanaroff-Riley Class I (FR I) radio galaxies NGC 193, B2 0206+35, B2 0755+37 and M 84 at frequencies of 4.9 and 1.4 GHz using new and archival multi-configuration observations from the Very Large Array. In addition, we describe lower-resolution observations of B2 0326+39 and a re-analysis of our published images of 3C 296. All of these radio galaxies show twin jets and well-defined lobes or bridges of emission, and we examine the common properties of this class of source. We show detailed images of total intensity, brightness gradient, spectral index, degree of polarization and projected magnetic-field direction. The jet bases are very similar to those in tailed twin-jet sources and show the characteristics of decelerating, relativistic flows. Except on one side of M 84, we find that the jets can be traced at least as far as the ends of the lobes, where they often form structures which we call "caps" with sharp outer brightness gradients. Continuing, but less well collimated flows back into the lobes from the caps can often be identified by their relatively flat spectral indices. The lobes in these radio galaxies are similar in morphology, spectral-index distribution and magnetic-field structure to those in more powerful (FR II) sources, but lack hot-spots or other evidence for strong shocks at the ends of the jets. M 84 may be an intermediate case between lobed and tailed sources, in which one jet does not reach the end of its lobe, but disrupts to form a "bubble".

Key words: galaxies: jets – radio continuum:general – magnetic fields – polarization

1 INTRODUCTION

Relativistic jets are the primary channel of energy loss from accreting supermassive black holes in many radio galaxies. They also have a major impact on their surroundings and act as accelerators of the most energetic photons (and perhaps hadrons) we observe. The present paper forms part of a study of jet physics in nearby, low-luminosity radio galaxies, specifically those with FR I morphology (Fanaroff & Riley 1974). We have developed a sophisticated model of FR I jets as relativistic, symmetrical, axisymmetric flows. By fitting to deep, high-resolution radio images in total intensity and linear polarization, we have determined the three-dimensional variations of velocity, emissivity and magnetic-field ordering in five sources (Laing & Bridle 2002a; Canvin & Laing 2004; Canvin et al. 2005; Laing et al. 2006b). We have shown that FR I jets decelerate from relativistic ($\beta = v/c \approx 0.8$) to subrelativistic speeds on scales of a few kpc and that they are faster on-axis than at their edges, as expected if they entrain external material.

The physics of boundary-layer entrainment must depend on the composition and density of the surrounding medium, and in particular on whether the jets propagate in direct contact with the intergalactic medium (IGM) or are surrounded by lobes consisting primarily of tenuous and at least partially relativistic plasma. Of the five sources we have modelled, three have *plumed* or *tailed* outer structures wherein most of the extended emission appears to lie further from the active nucleus than the narrower jets: 3C 31 (Laing & Bridle 2002a; Laing et al. 2008), B2 1553+24 (Canvin & Laing 2004; Young et al. 2005) and NGC 315 (Canvin et al. 2005; Laing et al. 2006a). We presume that their jets are in direct contact with the IGM. On the other hand, 3C 296 (Laing et al. 2006b) has two *lobes* with well-defined outer boundaries and a diffuse *bridge* of emission around the jets (at least in projection). A further source, B2 0326+39 (Canvin & Laing 2004), clearly has lobes, but it was unclear from published observations

⋆ E-mail: rlaing@eso.org

(Bridle et al. 1991) whether these lobes surround the inner jets.

Our best-fit model for the jets in the lobed FR I source 3C 296 (Laing et al. 2006b) is unusual in that it shows a very large transverse velocity gradient across the jet except very close to the nucleus, the ratio of edge to central velocity in this jet being $\lesssim 0.1$, compared with values ≈ 0.4 for the jets in three tailed sources (the value for 0326+39 is poorly determined). It is therefore of interest to examine whether jets in other FR I sources whose lobes entirely surround them appear to decelerate differently with distance from the nucleus than those in tailed FR I sources, or those in sources whose lobes may not extend all the way back to the nucleus, leaving the inner jets unshielded. Projection complicates interpretation of individual sources (the lobes may appear superimposed on the jets even if they are not in physical contact) and it is not always straightforward to separate jet and lobe emission, but the differences between 3C 296 and the rest are large. Modelling of the jets in a small number of lobed sources (which form the majority of complete samples of low-luminosity radio galaxies; Parma et al. 1996) should therefore be enough to decide whether there are systematic differences between the two classes.

The primary aim of this paper is to present high-quality radio imaging of four lobed FR I sources whose jets are suitable for modelling by our methods. The models themselves will be presented elsewhere. Our approach to jet modelling requires fitting to high-fidelity, deep images with linear resolution $\lesssim 0.25$ kpc derived from multi-configuration observations at 4.9 GHz (C-band) or 8.5 GHz (X-band) with the Very Large Array (VLA) at the National Radio Astronomy Observatory[1]. In order to correct the linear polarization for the effects of Faraday rotation (small at these frequencies), we also need to observe at several frequencies in the range 1.3 – 1.7 GHz (L-band). High-quality images of depolarization, rotation measure and spectral index are useful byproducts. In this paper, we describe:

(i) details of the observations,
(ii) the source morphologies in total intensity at a range of resolutions,
(iii) images of the spectral-index distributions and
(iv) images of the degree of polarization and the apparent magnetic field direction, corrected for Faraday rotation.

We also include high-resolution MERLIN[2] imaging for two of the sources. Faraday rotation and depolarization are analysed in detail by Guidetti et al. (2011, and in preparation).

We also present an analysis of the spectrum of 3C 296 which improves on that given by Laing et al. (2006b) and imaging of the large-scale structure of B2 0326+39 to trace its lobe emission closer to the nucleus than in earlier studies. These data complete the documentation of the large-scale structures and spectral-index distributions for all of the lobed FR I sources whose jets we can currently model.

[1] The National Radio Astronomy Observatory is a facility of the National Science Foundation operated under cooperative agreement by Associated Universities, Inc.
[2] MERLIN is a UK National Facility operated by the University of Manchester at Jodrell Bank Observatory on behalf of STFC.

Table 1. The sources. Col. 1: name (as used in this paper). Col. 2: alternative names. Col. 3: redshift. Col. 4: linear scale (kpc arcsec^{-1}) for our adopted cosmology. Col. 5: reference for redshift. Col. 6: reference for earlier observations of large-scale radio structure.

Name	Alternative	z	kpc arcsec^{-1}	Ref O	Ref R
NGC 193	PKS 0036+03 UGC 408	0.0147	0.300	9	4
0206+35	UGC 1651 4C 35.03	0.0377	0.748	3	8
0755+37	NGC 2484	0.0428	0.845	9	1
M 84	3C 272.1 NGC 4374	0.0035	0.073	10	5
3C 296	NGC 5532	0.0247	0.498	7	6
0326+39		0.0243	0.490	7	2

References: 1 Bondi et al. (2000), 2 Bridle et al. (1991), 3 Falco et al. (1999), 4 Giacintucci et al. (2011), 5 Laing & Bridle (1987), 6 Laing et al. (2006b), 7 Miller et al. (2002), 8 Morganti et al. (1987), 9 Ogando et al. (2008), 10 Trager et al. (2000).

Section 2 describes the new observations and data reduction, Section 3 presents our results for the sources individually, and Section 4 outlines the phenomenology of their jets and larger-scale emission as a prelude to modelling. Section 5 is a brief summary.

We adopt a concordance cosmology with Hubble constant, $H_0 = 70\,\mathrm{km\,s^{-1}\,Mpc^{-1}}$, $\Omega_\Lambda = 0.7$ and $\Omega_M = 0.3$.

2 OBSERVATIONS AND DATA REDUCTION

2.1 The sources

We selected four bright FR I sources for which available data suggested: (a) that full synthesis observations with the VLA would achieve signal-to-noise sufficient to image the linearly polarized emission from their counter-jets with several beamwidths resolution transverse to the radio features, as required by our modelling methods, and (b) that the jets have formed lobe-like structures rather than diffuse outer plumes. Three of the sources, NGC 193, B2 0206+35 and B2 0755+37 are analogous to 3C 296 in having well-defined outer boundaries. The fourth, M 84, is in some respects an intermediate case between the two classes, as we discuss below. We analysed a combination of new and archival datasets chosen to give good spatial-frequency coverage at two or three frequencies.

In addition, we improved our low-resolution images of 3C 296 (Laing et al. 2006b). Finally, we analysed shorter, low-resolution, archival VLA observations for B2 0326+39.

Alternative names, redshifts, linear scales and references for all of the sources are given in Table 1 (we drop the B2 from source names from now on). A journal of observations is given in Table 2[3].

[3] Laing et al. 2006b give a full description of the observations of 3C 296; this is not repeated here.

Table 2. Journal of VLA observations. Col. 1: source name. Col. 2: VLA configuration. Col. 3: Date of observation. Col. 4: centre frequencies for the one or two channels observed (MHz). Col. 5 bandwidth (MHz). Col. 6: the on-source integration time scaled to an array with all 27 antennas operational. Col. 7: VLA proposal code.

Source	Configuration	Date	ν [MHz]	$\Delta\nu$ [MHz]	t [min]	Proposal code
NGC 193	A	2007 Jun 02	4885.1, 4835.1	50	280	AL693
	A	2007 Jun 28	4885.1, 4835.1	50	90	AL693
	A	2007 Aug 22	4885.1, 4835.1	50	41	AL693
	A	2007 Aug 23	4885.1, 4835.1	50	88	AL693
	B	2007 Nov 05	4885.1, 4835.1	50	318	AL693
	B	2007 Nov 16	4885.1, 4835.1	50	121	AL693
	C	2008 May 24	4885.1, 4835.1	50	223	AL693
	D	2007 Mar 11	4885.1, 4835.1	50	53	AL693
	A	2007 Jun 28	1365.0	25	83	AL693
	A	2007 Aug 22	1365.0	25	39	AL693
	A	2007 Aug 23	1365.0	25	97	AL693
	B	2007 Nov 16	1365.0	25	148	AL693
	C	2008 May 24	1365.0	25	61	AL693
0206+35	A	2008 Oct 13	4885.1, 4835.1	50	486	AL797
	A	2008 Oct 18	4885.1, 4835.1	50	401	AL797
	B	2003 Nov 17	4885.1, 4835.1	50	254	AL604
	C	2004 Mar 20	4885.1, 4835.1	50	88	AL604
	A	2004 Oct 24	1385.1, 1464.9	25	189	AL604
	B	2003 Nov 17	1385.1, 1464.9	25	110	AL604
0755+37	A	2008 Oct 05	4885.1, 4835.1	50	477	AL797
	A	2008 Oct 06	4885.1, 4835.1	50	383	AL797
	B	2003 Nov 15	4885.1, 4835.1	50	332	AL604
	B	2003 Nov 30	4885.1, 4835.1	50	169	AL604
	C	2004 Mar 20	4885.1, 4835.1	50	125	AL604
	D	1992 Aug 2	4885.1, 4835.1	50	55	AM364
	A	2004 Oct 25	1385.1, 1464.9	12.5	450	AL604
	B	2003 Nov 30	1385.1, 1464.9	12.5	160	AL604
	C	2004 Mar 20	1385.1, 1464.9	12.5	21	AL604
M 84	A	1980 Nov 09	4885.1	50	223	AL020
	A	1988 Nov 23	4885.1, 4835.1	50	405	AW228
	A	2000 Nov 18	4885.1, 4835.1	50	565	AW530
	B	1981 Jun 25	4885.1	50	156	AL020
	C	1981 Nov 17	4885.1	50	286	AL020
	C	2000 Jun 04	4885.1, 4835.1	50	138	AW530
	A	1980 Nov 09	1413.0	25	86	AL020
	B	1981 Jun 25	1413.0	25	29	AL020
	B	2000 Feb 09	1385.1, 1464.9	50	30	AR402
0326+39	D	1997 Dec 13	4885.1, 4835.1	50	11	AR386
	D	1997 Dec 16	4885.1, 4835.1	50	32	AR386
	C	1998 Dec 4	1464.9, 1414.9	50	11	AR386
	D	1997 Dec 13	1464.9, 1385.1	50	6	AR386
	D	1997 Dec 16	1464.9, 1385.1	50	9	AR386

2.2 VLA data reduction

The VLA data listed in Table 2 were calibrated and imaged using the AIPS software package, following standard procedures with a few additions. The flux-density scale was set using observations of 3C 286 or 3C 48 and (except for 0326+39) the zero-point of **E**-vector position angle was determined using 3C 286 or 3C 138, after calibration of the instrumental leakage terms. The main deviations from standard methods were as follows.

Firstly, we used the routine BLCAL to compute closure corrections for the 4.9-GHz observations. This was required to correct for large closure errors on baselines between EVLA and VLA antennas in observations from 2007 onwards (VLA Staff 2010), but also improved a number of the earlier datasets. Whenever possible, we included observations of the bright, unresolved calibrator 3C 84 for this purpose; if it was not accessible during a particular observing run, we used 3C 286. We found that it was not adequate to use the standard calibration (which averages over scans) to compute the baseline corrections, as phase jumps during a calibrator scan caused serious errors in the derived corrections. We therefore self-calibrated the observations in amplitude and phase with a solution interval of 10 s before running BLCAL. We assumed a point-source model for 3C 84 and the well-determined CLEAN model supplied with the AIPS distribution for 3C 286.

Secondly, we imaged in multiple facets to cover the inner part of the primary beam at L-band and to image confusing sources at large distances from the phase centre in all bands.

Table 3. Resolutions and noise levels for the images used in this paper. Col. 1: source name. Col. 2: resolution (FWHM, in arcsec). Col. 3: frequency, in MHz. Col. 4: VLA configurations used in the image (not relevant for the two MERLIN observations). Cols 5 and 6: deconvolution method for I and Q/U images, respectively (MR: multi-resolution CLEAN; CL: single-resolution CLEAN; ME: maximum entropy). Cols 7 and 8: off-source noise levels. σ_I is the noise level on the I image; σ_P the average of the noise levels for Q and U. All noise levels were determined before correction for the primary beam response and larger values are appropriate at significant distances from the field centre. Col. 9: the approximate maximum scale of structure imaged reliably (Ulvestad, Perley & Chandler 2009). Cols 10 and 11: flux densities measured from the image and derived from single-dish measurements, respectively. The single-dish flux densities were taken from the references in Col. 12. They have been corrected as necessary to put them on the standard scale of Baars et al. (1977) and interpolated to our observing frequencies.

Source	FWHM [arcsec]	Freq [MHz]	Config-urations	Method I	Method QU	rms noise level [μJy beam^{-1}] σ_I	rms noise level [μJy beam^{-1}] σ_P	Max scale [arcsec]	$I_{\rm int}$/Jy Image	$I_{\rm int}$/Jy SD	Reference
NGC 193	0.45	4860.1	ABCD	ME	CL	8.6	8.2	300			
	1.35	4860.1	ABCD	MR	CL	7.1	7.4	300	0.79 ± 0.02	0.81 ± 0.04	3
	1.60	4860.1	ABCD	MR	CL	7.5	7.6	300	0.78 ± 0.02	0.81 ± 0.04	3
	1.60	1365.0	ABC	MR	MR	36	31	900	1.96 ± 0.04	1.84	7
	4.05	4860.1	ABCD	CL	CL	10	10	300	0.78 ± 0.02	0.81 ± 0.04	3
	4.05	1365.0	ABC	MR	MR	54	25	900	1.95 ± 0.04	1.84	7
0206+35	0.16	1658.0	MERLIN	CL	–	41	–	2.5			
	0.35	4860.1	ABC	MR	MR	7.2	7.1	300			
	1.20	4860.1	BC	MR	MR	12	12	300	0.90 ± 0.02	0.98 ± 0.12	2
	1.20	1464.9	AB	MR	MR	25	26	300	2.12 ± 0.04	2.13	5
	1.20	1385.1	AB	MR	MR	25	26	300	2.12 ± 0.04	2.22	5
	1.20	1425.0	AB	MR	–	19	–	300	2.12 ± 0.04	2.18	6
	4.50	4860.1	BC	MR	–	18	–	300	0.90 ± 0.02	0.98 ± 0.12	2
	4.50	1425.0	AB	MR	–	38	–	300	2.13 ± 0.04	2.18	6
0755+37	0.14	1658.0	MERLIN	CL	–	68	–	2.5			
	0.40	4860.1	ABCD	MR	MR	8.0	7.1	300			
	1.30	4860.1	BCD	MR	MR	7.8	7.9	300	1.26 ± 0.03	1.27 ± 0.02	4
	1.30	1464.9	ABC	MR	MR	28	28	300	2.60 ± 0.05	2.53 ± 0.09	4
	1.30	1385.1	ABC	MR	MR	27	26	300	2.74 ± 0.05	2.62 ± 0.09	4
	1.30	1425.0	ABC	MR	–	20	–	300	2.64 ± 0.05	2.57 ± 0.09	4
	4.00	4860.1	BCD	MR	MR	14	12	300	1.25 ± 0.03	1.27 ± 0.02	4
	4.00	1464.9	ABC	MR	MR	44	42	300	2.59 ± 0.05	2.53 ± 0.09	4
	4.00	1385.1	ABC	MR	MR	46	36	300	2.73 ± 0.05	2.62 ± 0.09	4
	4.00	1425.0	ABC	MR	MR	32	–	300	2.65 ± 0.05	2.57 ± 0.09	4
M 84	0.40	4860.1[a]	ABC	MR	MR	11	10	300			
	1.65	4860.1[a]	ABC	MR	MR	15	11	300	2.94 ± 0.06	2.88 ± 0.08	5
	1.65	1413.0	AB	MR	MR	140	140	120	6.03 ± 0.12	6.44 ± 0.24	5
	4.5	4860.1[a]	C	MR	MR	23	20	300	2.98 ± 0.06	2.88 ± 0.08	5
	4.5	1464.9	B	MR	MR	120	70	120	6.14 ± 0.12	6.32 ± 0.24	5
	4.5	1413.0	AB	MR	MR	210	150	120	5.99 ± 0.12	6.44 ± 0.24	5
	4.5	1385.1	B	MR	MR	130	69	120	6.46 ± 0.13	6.51 ± 0.24	5
3C 296	5.5	8460.1	ABCD	MR	–	14	–	180	1.34 ± 0.03	1.20 ± 0.10	5
	5.5	1479.0	BCD	MR	–	24	–	900	4.10 ± 0.08	4.08 ± 0.18	5
0326+39	18.0	4860.1	D	CL	–	47	–	300	0.60 ± 0.01	0.62 ± 0.09	1
	18.0	1425.0	CD	CL	–	140	–	900	1.47 ± 0.03	1.30	6

References: 1 Becker, White & Edwards (1991), 2 Gregory & Condon (1991), 3 Griffith et al. (1995), 4 Kühr et al. (1981), 5 Laing & Peacock (1981), 6 White & Becker (1992), 7 Wright & Otrupcek (1990).

[a] Although the 1980 and 1981 observations have a centre frequency of 4885.1 MHz, the weighted mean for the combined dataset is still close to 4860.1 MHz

Before combining configurations, we subtracted in the (u, v) plane all sources outside a fixed central field. For 0755+37 at L-band, this procedure failed to remove sidelobes at the centre of the field from a bright confusing source close to the half-power point of the primary beam. The reason is that the VLA primary beam is not azimuthally symmetric, so the effective complex gain for a distant source is not the same as that at the pointing centre and varies with time in a different way. We used the AIPS procedure PEELR to remove the offending source from the (u, v) data for each configuration before combining them.

Finally, we corrected for variations in core flux density and amplitude scale between observations as described in Laing et al. (2006b).

J2000 coordinates are used throughout this paper. If positions from archival data were originally in the B1950 system, then (u,v,w) coordinates were recalculated for J2000 before imaging. The astrometry for each of the sources was set using the A-configuration observations, referenced to a

nearby phase calibrator in the usual manner. Thereafter, the position of the compact core was held constant during the process of array combination.

The observations of M 84 in 1980 and 1981 used an earlier and less accurate value of the position of the phase calibrator B1236+077 (alias J1239+075) than that currently given in the VLA calibrator manual. We have updated the astrometry to reflect the improved calibrator position. The archival L-band observations of M 84 taken in 2000 used a pointing centre displaced by ≈1.1 arcmin from the centre of the source.

The C-band data were usually taken in two adjacent 50-MHz frequency channels, which were imaged together. The L-band channels were also imaged together in I, in order to derive spectral-index images. For all sources except 0326+39, they were also imaged independently, primarily for analysis of linear polarization.

In order to avoid the well-known problems introduced by the conventional CLEAN algorithm for well-resolved, diffuse brightness distributions, total-intensity images at the higher resolutions were produced using the multi-scale CLEAN algorithm as implemented in the AIPS package (Greisen et al. 2009) or, in one case, a maximum-entropy algorithm (Cornwell & Evans 1985, used as described by Leahy & Perley 1991). The standard single-resolution CLEAN was found to be adequate for the lowest-resolution I images. Stokes Q and U images were CLEANed using one or more resolutions (we found few differences between single and multiple-resolution CLEAN for these images, which have little power on large spatial scales). All of the images were corrected for the effects of the antenna primary beam.

In general, the deep 4.9-GHz images have off-source noise levels very close to those expected from thermal noise in the receivers alone. There are a few faint artefacts on the I images. These are visible as concentric rings around the bright cores and, for NGC 193 at 1.35 and 1.6-arcsec resolution, a quadrupolar pattern at the 2σ level. These are due to errors in cross-calibration of the different array configurations, which were particularly troublesome due to the low declination of this source. The integrations for all of the L-band images and for the C-band image of 0326+39 are shorter and confusion from sources outside the field of view is worse, so noise levels are correspondingly higher.

Finally, we produced improved I images from self-calibrated L- and X-band visibility data for 3C 296 (Laing et al. 2006b) using the multi-resolution CLEAN algorithm.

As a check on the amplitude calibration and imaging of the I images used in spectral-index analysis, we integrated the flux densities using the AIPS verb TVSTAT. We estimate that our errors are dominated by a residual scale error of ≈2%. All of the results are in excellent agreement with single-dish measurements (Table 3).

The configurations, resolutions, deconvolution algorithms and noise levels for the final images are listed in Table 3. The noise levels were measured before correction for the primary beam, and are appropriate for the centre of the field.

2.3 MERLIN observations and reduction

We also present MERLIN imaging in total intensity only for two of the sources. 0206+35 was observed for a total time of about 14 hours. The array included the following telescopes: Defford, Cambridge, Knockin, Wardle, Darnhall, Mk2, Lovell and Tabley. The observations were carried out at 1420 MHz with a bandwidth of 15 MHz, in each of left and right circular polarizations. The nearby compact source 0201+365 was used as the phase calibrator and the flux-density scale was determined using 3C 286. The data were edited, corrected for elevation-dependent effects and non-closing errors and flux-calibrated using the standard MERLIN analysis programs. Imaging and self-calibration were again performed using the AIPS package. The off-source image rms after self-calibration was close to that expected from receiver noise alone. The MERLIN observations of 0755+37 were described by Bondi et al. (2000).

The parameters of both MERLIN images are given in Table 3.

3 IMAGES

3.1 General

Our conventions for Figs 1 – 12 and the descriptions in the text are as follows.

(i) Images of total intensity, I, are shown as grey-scales, over ranges indicated by the labelled wedges. The units are mJy beam^{-1}.

(ii) We also show grey-scales of intensity gradient, $|\nabla I|$, approximated using a Sobel filter (Sobel & Feldman 1968).

(iii) We use the notation $P = (Q^2 + U^2)^{1/2}$ for polarized intensity and $p = P/I$ for the degree of linear polarization. p_ν is the degree of polarization at frequency ν (in GHz). All values of P have been corrected for Ricean bias (Wardle & Kronberg 1974). Linear polarization is illustrated by plots in which vectors with lengths proportional to the degree of polarization at 4.9 GHz ($p_{4.9}$) and directions along the apparent magnetic field ($\mathbf{B}_\mathrm{a}$) are superposed on false-colour images of either I (again with a labelled wedge indicating the range) or $|\nabla I|$. A value of $p = 1$ is indicated by the labelled bar. The apparent field direction is $\chi_0 + \pi/2$, where χ_0 is the **E**-vector position angle corrected to zero-wavelength by fitting to the relation $\chi(\lambda^2) = \chi_0 + \mathrm{RM}\lambda^2$ for foreground Faraday rotation derived from the images in Table 3 (RM is the rotation measure). In some sources, we used RM images at lower resolution to correct the position angles, as detailed in the captions. This procedure is valid if the RM varies smoothly over the low-resolution image, and maximises the area over which we can determine the direction of the apparent field. Vectors are plotted where: (a) $I \geq 5\sigma_I$, (b) $P \geq 3\sigma_P$ (the noise levels are given in Table 3) and (c) the RM is well-determined. The RM images for 0206+35 and M 84 were determined using three and four frequencies, respectively and are shown in Guidetti et al. (2011); that for 0755+37 (also from three frequencies) will be described by Guidetti et al. (in preparation). For NGC 193, images were only available at 4.86 and 1.365 GHz. The integrated RM of the source is small (-18 ± 2 rad m^{-2}; Simard-Normandin, Kronberg & Button

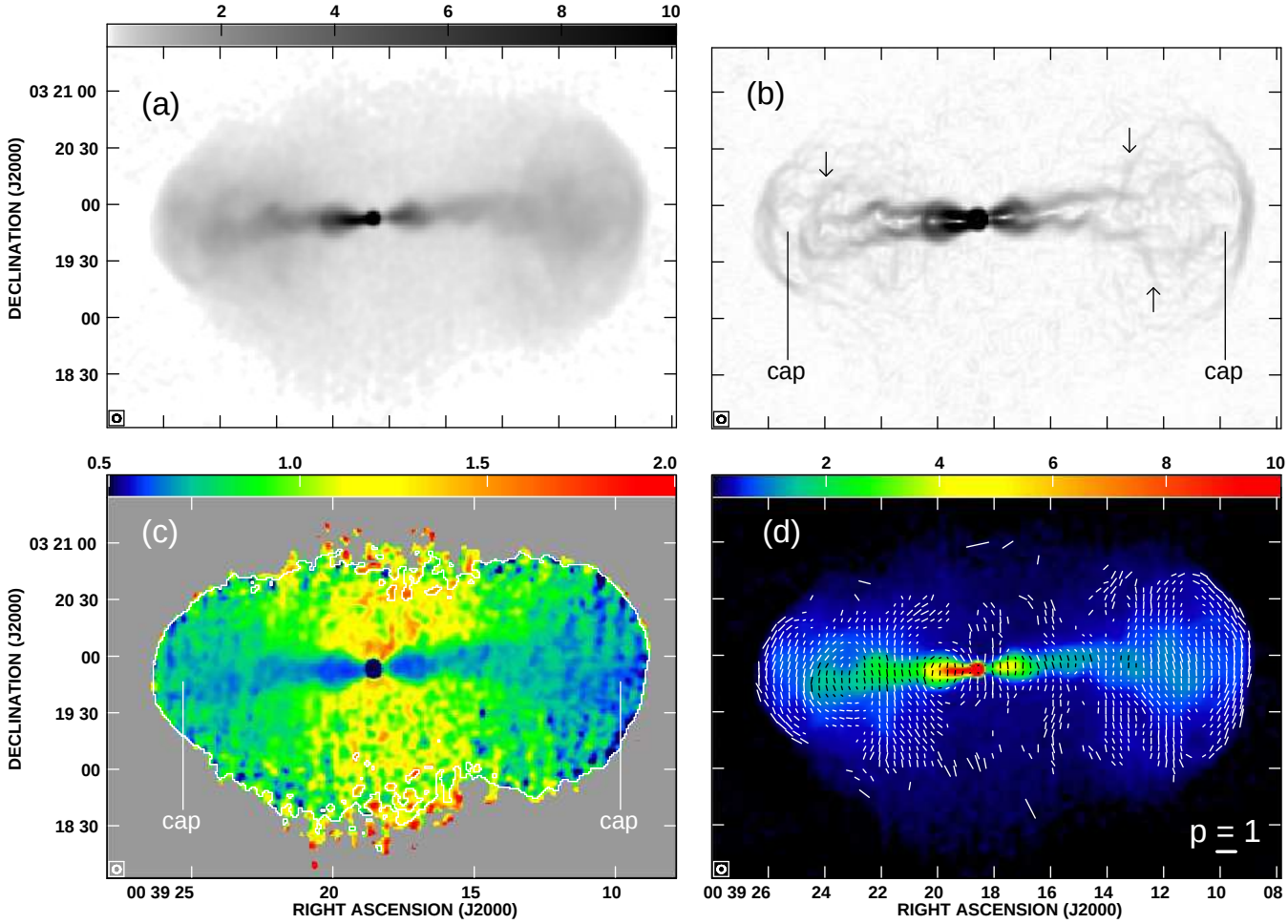

Figure 1. Images of NGC 193 at 4.05-arcsec resolution. (a) Total intensity at 4.9 GHz. (b) Intensity gradient for the image in panel (a). The arrows mark the high brightness gradients which coincide with the edges of the flat-spectrum caps (which are also marked). (c) Spectral-index image between 4.9 and 1.4 GHz. Values outside the white contour are lower limits. The caps are indicated. (d) Vectors with directions along $\mathbf{B}_{\rm a}$ and magnitudes proportional to $p_{4.9}$, plotted on a false-colour image of total intensity at 4.9 GHz.

1981) as are the variations of position-angle difference across the source. We are therefore confident that a two-frequency RM determination is adequate in this case (the correction required to derive $\mathbf{B}_{\rm a}$ is in any case very small).

(iv) Spectral index, α, is defined in the sense $S(\nu) \propto \nu^{-\alpha}$ and we use $\alpha_{\nu_1}^{\nu_2}$ for the index between frequencies ν_1 and ν_2 (in GHz). In the false-colour images of spectral index, the input I images at the lower frequency are always blanked for $I < 3\sigma_I$.[4] In cases where the areas over which emission was detected were essentially the same at both frequencies, we also blanked the higher-frequency image at $3\sigma_I$. If significant areas were detected only at the lower frequency, we did not blank the higher-frequency image. Instead, we plot a single contour which indicates the boundary of the region where the source is detected at $I \geq 3\sigma_I$ at the higher frequency. Outside this contour, the spectral indices are lower limits. We have carefully inspected the spectral-index images to check for edge effects and zero-level problems. We are confident that the values and lower limits in all of the unblanked regions are reliable except where explicitly stated and that the steep spectra seen at the edges of the lobes in several sources are real.

(v) The restoring beam (FWHM) is shown at the bottom of each plot.

(vi) We refer to parts of the sources by the abbreviations N, S, E, W (for North, South, East, West) etc.

(vii) We refer to the *main* (brighter) and *counter* (fainter) jets.

3.2 NGC 193

Fig. 1(a) shows the total-intensity distribution over NGC 193 at 4.9 GHz and 4.05-arcsec FWHM resolution. The symmetrical jets appear to broaden rapidly and also bend away from their initial straight path as they reach the midpoints of symmetric lobes. The lobes both have well-defined leading edges that approximate arcs of circles in projection on the sky (the W lobe having a larger radius of curvature), but they lack hot spots that might mark the termination points of the jets. A broad, faint emission bridge fills the central region of the source between the lobes and appears

[4] The spectral-index image for M 84 has additional blanking, as noted in the caption of Fig. 9(c)

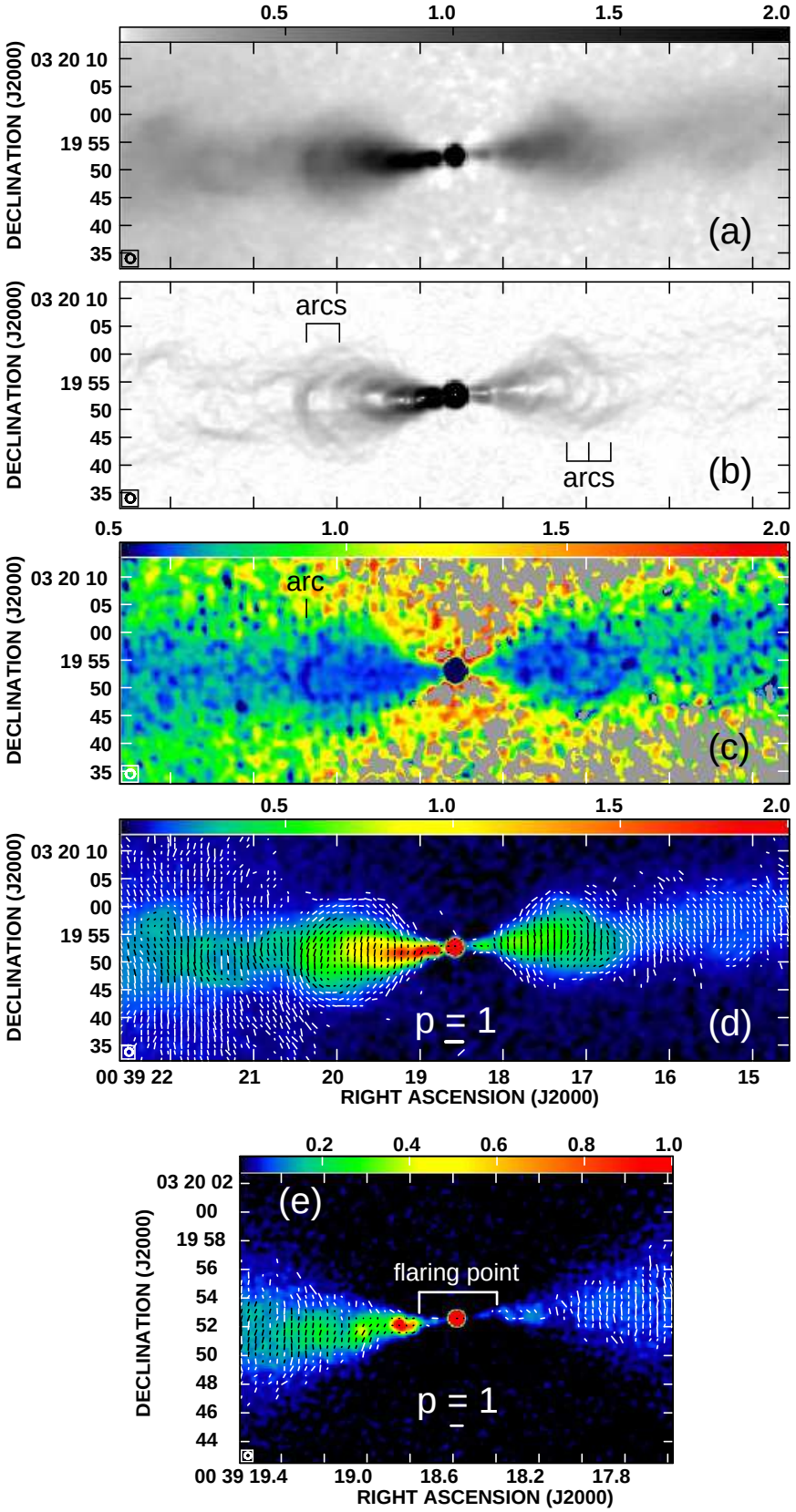

Figure 2. High-resolution images of the inner jets of NGC 193. (a) Total intensity at 4.9 GHz with 1.6 arcsec FWHM resolution. (b) Brightness gradient derived from the image in (a). Sharp steps in brightness ("arcs") are indicated. (c) Spectral index between 4.9 and 1.4 GHz at 1.6-arcsec resolution. The most prominent of the arcs, which shows a flattening in spectral index, is marked. (d) Vectors with directions along $\mathbf{B}_{\rm a}$ and magnitudes proportional to $p_{4.9}$, plotted on false-colour images of total intensity at 4.9 GHz with 1.35 arcsec FWHM resolution. The vectors have been corrected for Faraday rotation using a 4.05-arcsec FWHM resolution RM image. (e) As in panel (d), but for the innermost jet regions at 0.45-arcsec resolution.

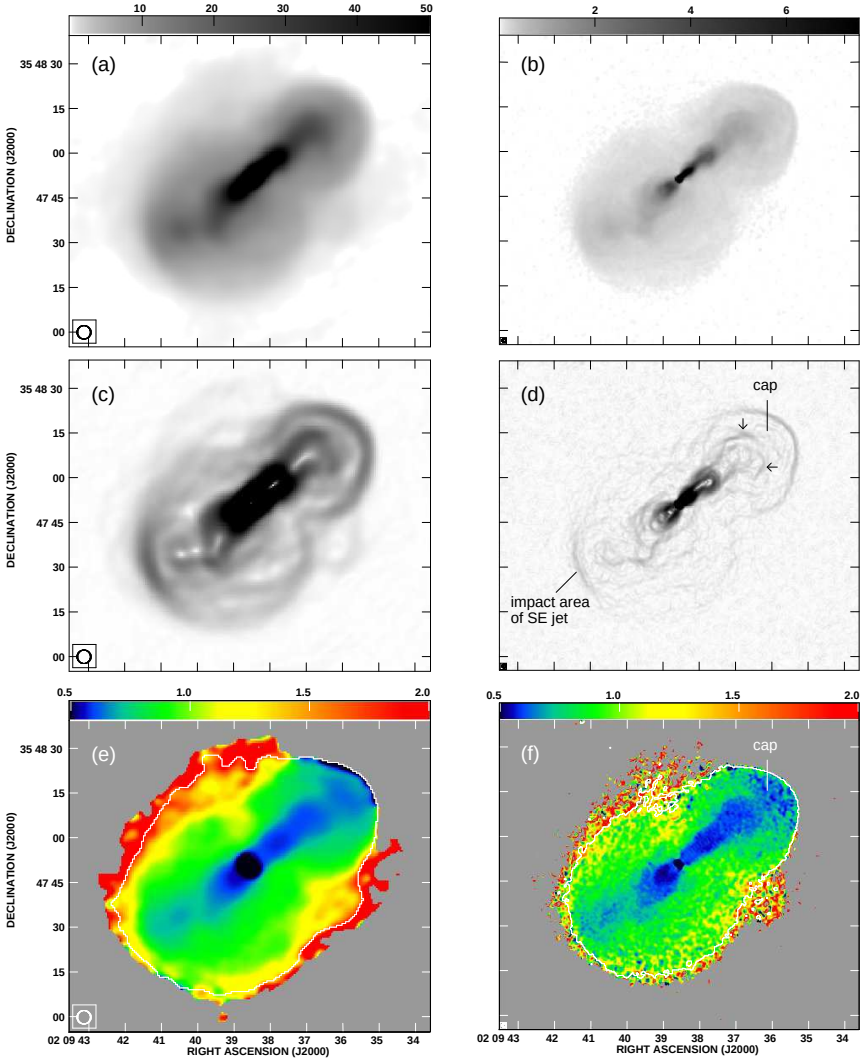

Figure 3. Images of 0206+35. (a) Total intensity at 1.4 GHz with 4.5-arcsec FWHM resolution. (b) Total intensity at 4.9 GHz, 1.2-arcsec FWHM. (c) Intensity gradient at 1.4 GHz, 4.5-arcsec FWHM. (d) Intensity gradient at 1.4 GHz, 1.2-arcsec FWHM. The arrows mark the high brightness gradients around the inner boundary of the flat-spectrum cap. (e) Spectral index between 4.9 and 1.4 GHz, 4.5-arcsec FWHM. (f) Spectral index between 4.9 and 1.4 GHz, 1.2-arcsec FWHM. In panels (e) and (f), values outside the contours are lower limits.

to be wider than the lobes in the N-S direction in the centre of the source (similar to the "wings" observed in some FR II sources; Cheung 2007, and references therein). Figs 1(b) and (c) taken together show that broad "caps" of emission can be delineated in both lobes by enhanced intensity gradients and by lower-than-average values of $\alpha_{1.4}^{4.9}$. The intensity gradients are largest at the outer edges of these caps, but there are also gradient features within the lobes (marked with arrows on Fig. 1b) which coincide with the edges of the flatter-spectrum region. The regions where the jets are most prominent have low spectral indices around 0.6. The spectral index at the trailing edges of the caps steepens smoothly to $\alpha \approx 0.9$ where the emission merges with the broader, symmetric lobes. The most diffuse lobe emission has spectral indices increasing from ≈1 at the edges of the most elongated parts of the lobes to ≈1.4 near the centre of the source, a spectral-index pattern characteristic of lobed radio sources of both FR classes (see Section 4.2). There are regions of emission with spectral index approaching 2 at the edges of the faintest emission on the N and S edges of the source.[5] Fig. 1(d) shows that the distribution of the apparent magnetic field direction over the lobes is basically circumferential, while the magnetic field in the jets is perpendicular to the jets over most of their lengths. The structure of the apparent magnetic field in both the jets and the lobes appears regular, and characteristic of that commonly found in jets of FR I sources and in the lobes of both FR classes.

Fig. 2(a) shows the total-intensity distribution over the jets at 4.9 GHz with a resolution of 1.6 arcsec FWHM. Both jets are fairly straight and similar in overall appearance, exhibiting rapid lateral expansion just beyond the distance from the unresolved nuclear radio source at which the E jet is markedly brighter than the W jet. Their edges are well

[5] The spectral index within a few arcsec N and S of the core is affected by artefacts in the 4.9-GHz image.

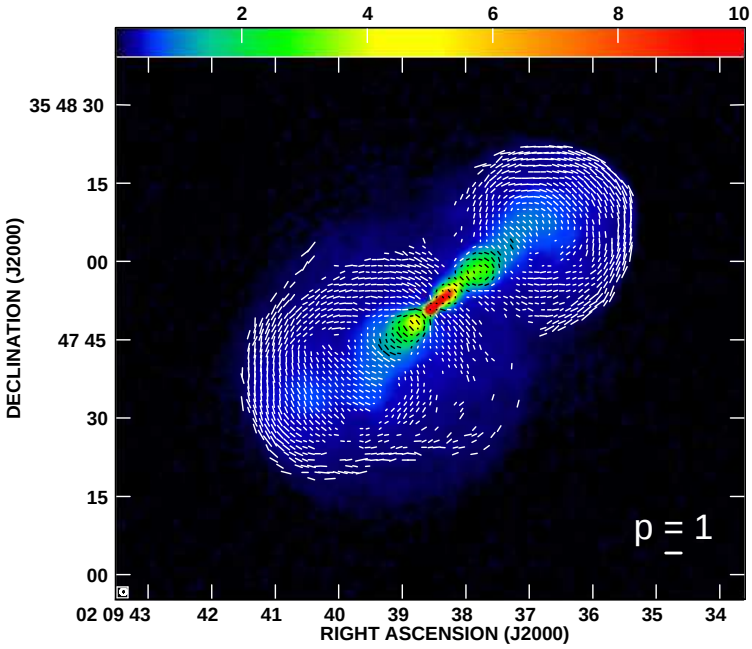

Figure 4. Vectors with directions along the apparent magnetic field and lengths proportional to the degree of polarization at 4.9 GHz, superimposed on a false-colour image of total intensity across 0206+35 at the same frequency. The resolution is 1.2 arcsec FWHM. The apparent field directions were derived using a three-frequency rotation-measure fit (Guidetti et al. 2011).

delineated by steep transverse intensity gradients near the midpoint of the source (Fig. 2b). The surface brightnesses of both jets decrease smoothly with distance from the nucleus except at a distance of ≈25 arcsec, where there are more sudden drops, mostly clearly visible as "arcs" crossing the jets on the gradient image (indicated on Fig. 2b). The overall spectral index of the jet-dominated emission appears to steepen with distance from the nucleus, but this is almost certainly the result of superposition of dimming jets on steeper-spectrum lobe emission. The prominent arc in the E jet is associated with a slight flattening in the spectrum (Fig. 2c).

Fig. 2(d) shows the intensity and apparent magnetic field distributions over the inner ≈45-arcsec regions of both jets at 1.35-arcsec resolution. The magnetic field organization over both jets is quite regular, with the field closest to the jet axis predominantly orientated perpendicular to the axis. The apparent field at the edges of the inner jets is parallel to the rapidly-expanding outer isophotes. Farther from the nucleus, the edge field directions in both jets converge towards the axis to form almost circular patterns.

Fig. 2(e) shows the 4.9-GHz total intensity and apparent magnetic-field distributions over the inner 15 arcsec (≈4.5 kpc) of the jets at 0.45-arcsec resolution. Both jets exhibit faint inner regions in the first ≈2 arcsec from the nucleus before they brighten and subsequently flare. There is bright, non-axisymmetric knot structure in the first ≈4 arcsec of the E jet, downstream of the flaring point (Laing et al. 1999), where both jets brighten abruptly.

3.3 0206+35

Fig. 3 shows the total-intensity, brightness gradient, and spectral-index distributions over the whole of 0206+35 at two resolutions. Fig. 3(a) at 1.4 GHz, 4.5-arcsec FWHM resolution, shows that the large scale structure consists of two lobes, overlapping and circular in cross-section, with well-defined outer edges to the NW and SE of the source, superimposed on fainter diffuse emission to the N and S. Fig. 3(b), at 4.9 GHz and 1.2-arcsec resolution, shows the source in more detail but with reduced sensitivity to the largest-scale emission. At this resolution, both lobes show sharp outer boundaries. The roughly circular edge of the NW lobe protrudes beyond the diffuse emission, whereas the corresponding feature in the SE is well inside the outer boundary of the source and is most obvious in the E of the lobe, close to the termination of the jet. If the orientation of $\theta \approx 40^\circ$ determined for the inner jets (Laing & Bridle, in preparation) also applies to the lobes, then they are presumably ellipsoidal with an axial ratio ≈1.6. Fig. 3(b) also shows some internal structure in both jets. The NW jet has the brighter base, and both bends and brightens as it enters its lobe, after which its path meanders. The SE counter-jet appears to expand more rapidly initially, then also meanders as it enters its lobe.

Figs 3(c) and (d) show the 1.4-GHz intensity gradient images of 0206+35 at 4.5-arcsec and 1.2-arcsec resolution, respectively. The edges of the jets are clearly marked by enhanced intensity gradients at both resolutions, while significant internal structure is also apparent in the lobes. Both lobes exhibit strong brightness gradients at their outer edges in these displays, corresponding to the sharp boundaries noted earlier. There is a particularly striking correlation between the main features of these intensity-gradient images and of the two 1.4 to 4.9-GHz spectral-index images shown as Figs. 3(e) and (f). The emission inside the brightest intensity gradients around the jet has a much lower spectral index, typically <0.65, than the ≈0.7 to 1.0 spectral index

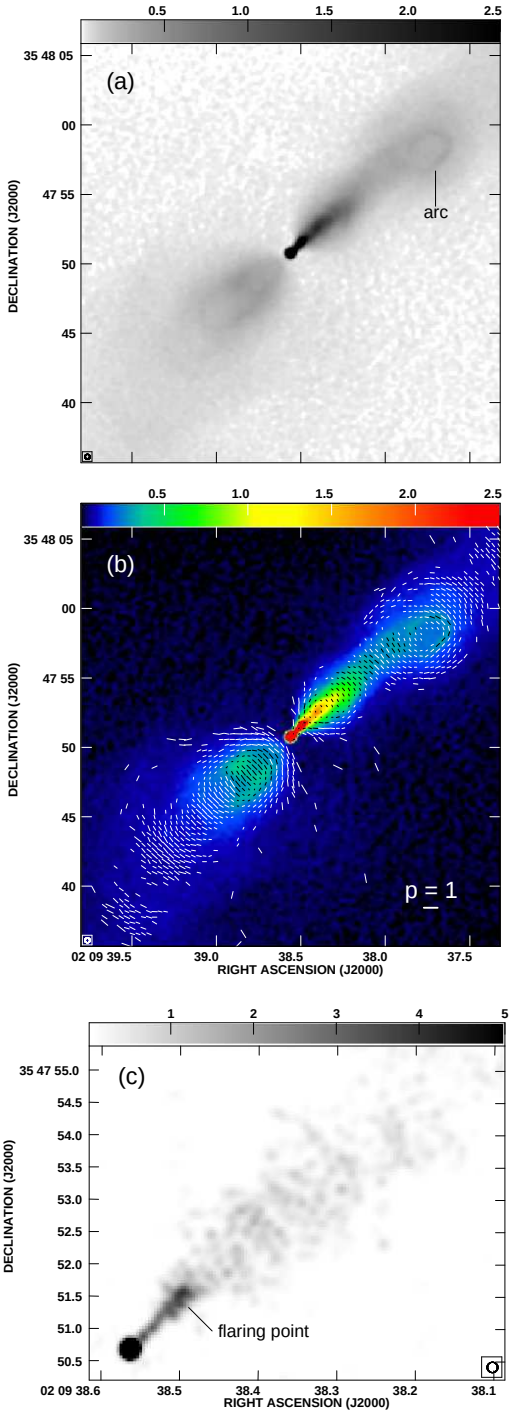

Figure 5. (a) Grey-scale of the 4.9-GHz total-intensity distribution over the jets in 0206+35 at 0.35-arcsec FWHM resolution. The grey-scale range is 0 – 2.5 mJy beam^{-1}. (b) Vectors with lengths proportional to the degree of polarization at 4.9 GHz and directions along the apparent magnetic field, superimposed on a false-colour display of the total intensity at 4.9 GHz. The resolution is 0.35 arcsec FWHM. The vector directions are derived from 3-frequency RM fits at 1.2-arcsec resolution. (c) Grey-scale of the 1.6-GHz total intensity distribution over the inner 5 arcsec of the NW jet and the unresolved nuclear source in 0206+35 at 0.16-arcsec FWHM resolution, from MERLIN. The grey-scale range is 0 – 5 mJy beam^{-1}.

that is prevalent over the rest of the two spherical lobes. The diffuse emission outside the lobes has spectral indices ranging from ≈1.05 to >2, generally increasing with distance from the lobes towards the outer edge of the source. Also notable are the "fans" of lower-spectral-index emission that can be traced from the ends of the jets to the regions at the edges of both lobes that show the most pronounced brightness gradients. This is particularly striking in the NW lobe, where a cap of lower-spectral-index emission is bounded by the high brightness gradients marked by arrows on Fig. 3(d) and by the edge of the lobe. This suggests that the jet outflow has reached the end of the lobe in a less-collimated, but still identifiable, form. In the SE lobe, the jet bends to the N before appearing to impact the edge of the lobe at another enhanced brightness gradient, marked in Fig. 3(d).

Fig. 4 shows that the magnetic field configuration in both lobes is well ordered and basically circumferential, while the magnetic field in the jets is predominantly perpendicular to their axis near the centre lines of the jets, with evidence for parallel field at the jet edges. The southern edge of the source is strongly polarized with field tangential to the boundary.

At 0.35-arcsec FHWM resolution (Fig. 5a) the lobe emission is substantially resolved out so the images are dominated by the jets. The bright base of the main (NW) jet is clearly centre-brightened, while the corresponding segment of the counter-jet appears centre-darkened. While at first sight the main jet appears to expand more slowly than the counter-jet, *the geometry of the centre-darkened segment of the counter-jet is very similar to that of the main jet over the first ≈10 arcsec*. This suggests a two-component view of these jets wherein a narrow inner structure, brighter to the NW and fainter to the SE, is seen superposed on a broader expanding structure that is slightly brighter to the SE than to the NW. We will interpret this elsewhere (Laing & Bridle, in preparation) as evidence for a symmetrical relativistic outflow surrounded by a mildly relativistic backflow in this source.

The magnetic field is clearly perpendicular to the jet axis over most of the length of both jets (Fig. 5b), but the first few arcsec of the main jet, where it is brightest, have the magnetic field parallel to the jet axis. There is also evidence for oblique, or parallel, magnetic field at the edges of both jets.

Fig. 5(c) shows the bright, narrow base of the NW jet from MERLIN data at 1.6 GHz. This higher-resolution (0.16 arcsec FWHM) image unambiguously identifies the flaring point in the jet, 0.7 arcsec from the nucleus, where it brightens abruptly. This is an important fiducial distance for our modelling. The image also shows the start of rapid expansion downstream of the flaring point.

3.4 0755+37

Fig. 6 shows the total-intensity, $|\nabla I|$ and α distributions over all of 0755+37 at two resolutions and the polarization at low resolution. Fig. 6(a) at 1.4 GHz, 4.0-arcsec FWHM resolution, shows that the large-scale structure consists of two lobes, again roughly circular in projection, with well-defined but not particularly sharp outer edges to the W and E, plus fainter diffuse emission to the N and S. The E lobe has a series of narrow ridges and brightness steps, all roughly arcs of

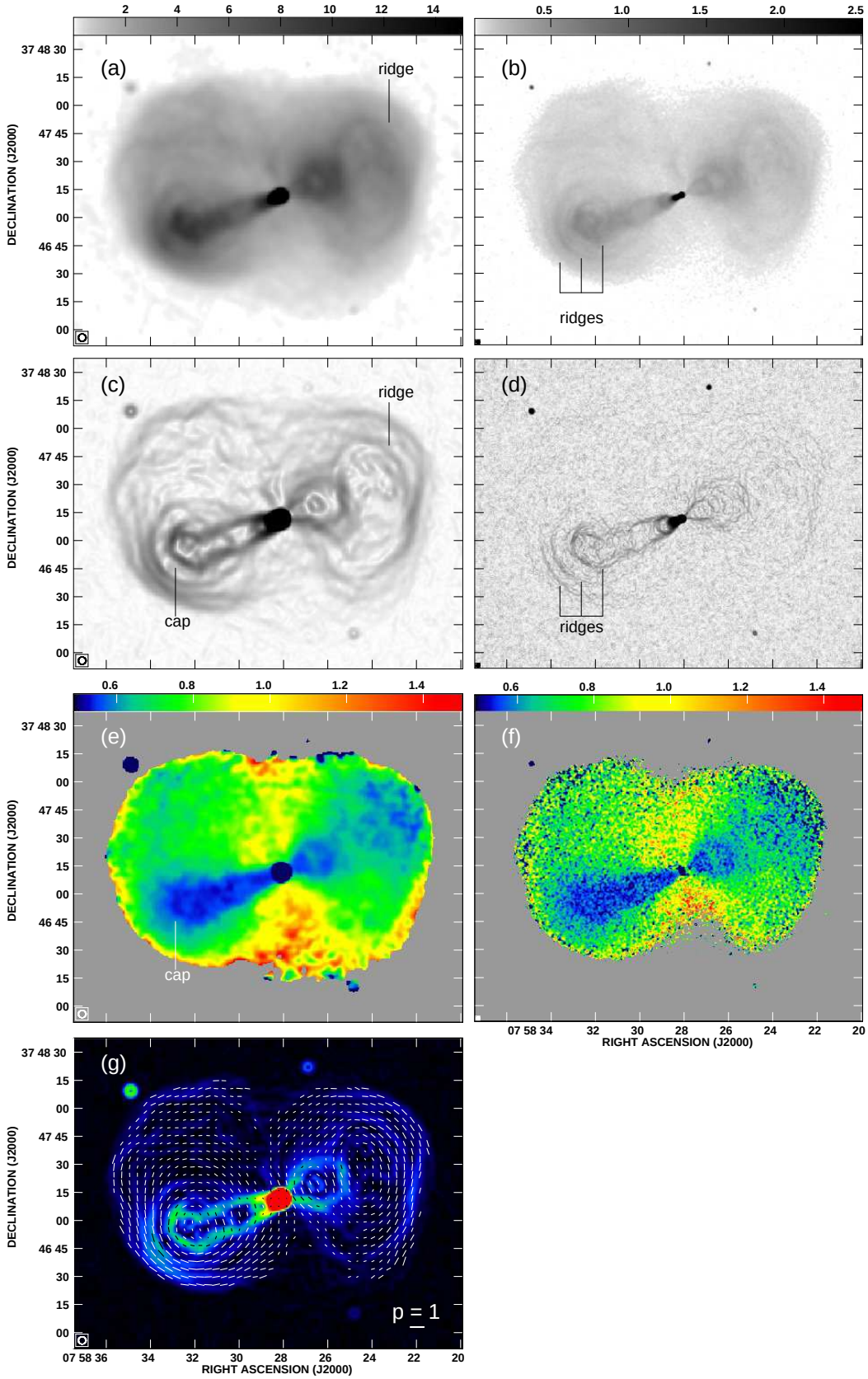

Figure 6. Images of the whole of 0755+37 at resolutions of 4.0 arcsec FWHM (panels a, c, e and g) and 1.3 arcsec FWHM (panels b, d and f). (a) Total intensity at 1.4 GHz. (b) Total intensity at 4.9 GHz. (c) Intensity gradient at 1.4 GHz. (d) Intensity gradient at 4.9 GHz. (e) and (f) spectral index between 4.9 and 1.4 GHz. (g) vectors with lengths proportional to $p_{4.9}$ and directions along the apparent magnetic field from a three-frequency rotation-measure fit (Guidetti et al., in preparation), superimposed on the intensity gradient at 4.9 GHz.

circles in projection, in the region where the brighter jet appears to terminate. They are recessed from the E boundary of this lobe and some may be the edges of thin shells. The structure of the W lobe is unusual, containing some arc-like features and other structure suggestive of a rapidly decollimating counter-jet W of the nucleus, as previously described by Bondi et al. (2000), with a "hole", or deficit of emission in the region where the counter-jet might be expected to terminate. Fig. 6(b) at 4.9 GHz, 1.3-arcsec FWHM resolution, is insensitive to the largest scales of emission to the N and S of the main source, but clearly shows internal structure in the E lobe, including the concentric semicircular ridges at the end of the jet (labelled on the figure). All of the substructure in the W lobe appears to be resolving out, though vestiges of the ridge apparent at lower resolution in Fig. 6(a) remain.

Figs. 6(c) and (d) show the intensity gradients over the whole source at 1.4 GHz, 4.0 arcsec FWHM resolution and 4.9 GHz, 1.3 arcsec FWHM resolution, respectively. These figures emphasise the strong differences between the internal structures of the lobes: multiple recessed ridges with significant brightness gradients in the E lobe, but much smoother structure in the W lobe away from the jet.

Figs. 6(e) and (f) clearly show three distinct spectral-index regions on each sides of the source, as follows.

(i) $\alpha \approx 0.6$ at the bases of both jets, in a broad cap in the NW part of the W lobe, and all along the region delineated by the strongest brightness gradients in the E jet.

(ii) $\alpha \approx 0.8$ over most of the rest of both lobes, including the ridge extending Northward from the nucleus.

(iii) There is also steeper-spectrum diffuse emission with α increasing from ≈ 1 in the central part of the source to $\approx$1.5 at the N and S edges.

The spectral-index image suggests that the counter-jet flow persists as far as the ridge of emission in the W lobe marked on Figs. 6(a) and (b), despite the lack of evidence for this in total intensity.

Fig. 6(g) shows that the apparent magnetic field in both lobes is exceptionally well organised, and mainly tangential to the lobe boundaries. The degree of linear polarization is $p \gtrsim 0.6$ over much of both lobes, consistent with the high degree of organization evident from the vectors. Note the excellent alignment between the field vectors and the ridges of high brightness gradient on both sides of the source. Fig. 7 confirms the exceptional degree of ordering of the magnetic field in both lobes at 1.3-arcsec FHWM resolution.

Fig. 8 shows the jet bases on larger scales and at higher resolution. Fig. 8(a) is optimised to emphasise fine-scale structure in the jets at 1.3-arcsec resolution. It shows that the E jet has the brighter base but becomes limb-brightened at the position indicated on Fig. 8(a) at about 18 arcsec from the nucleus. At this resolution, the W counter-jet contains a centre-darkened structure that expands at about the same rate as the brighter E jet, embedded in a much broader, and more rapidly-expanding cone of emission with at least two curved arcs (Fig. 8a). The centre of the counter-jet is crossed by a prominent, straight bar of emission (labelled as such on Fig. 8a) at $\approx$15 arcsec from the core. The steepest brightness gradients at the edges of both jets are very similar in form within $\approx$15 arcsec of the nucleus so that, as in 0206+35, the *inner* geometry of the counter-jet structure appears to mimic that of the brighter jet on the other side of the source (Fig. 8b).

Fig. 8(b) also shows detail of the magnetic field organisation at the bases of both jets at 1.3-arcsec resolution. The bright base of the E jet has the magnetic field roughly parallel to the jet axis, but there is a rapid transition, with the field becoming perpendicular to the axis as the jet expands. On the counter-jet side the field is also transverse. There is little evidence for any perturbation of the magnetic field structure at the edges of the jets except at the N edge of the counter-jet where the magnetic field becomes parallel to the steepest brightness gradient once the jet widens significantly. The very high degree of polarization in the surrounding diffuse emission makes it difficult to disentangle the true polarization of the jets where their emission is weak, e.g. at their edges.

Figs 8(a) and (b) also show a filament of faint emission which extends for about 30 arcsec Northward from the vicinity of the nuclear source, roughly perpendicular to the jets. It has a very high degree of linear polarization, with an apparent magnetic field parallel to its length. Fig. 7 suggests that this highly polarized filament may be part of a larger region of enhanced polarization that delineates the inner boundary of the W lobe.

Fig. 8(c) shows the total-intensity structures at the bases of the jets at 0.4 arcsec resolution. The main jet is clearly centre-brightened whereas the counter-jet is not and the brighter edges of the counter-jet lie mostly outside the region that would be delineated by reflecting the main jet across the nucleus. As in 0206+35 (Fig. 5a) there is a narrow collimated structure within which the main jet is systematically brighter than the counter-jet apparently superposed on a broader structure which is brighter around the counter-jet than around the main jet. As for 0206+35, we will show elsewhere (Laing & Bridle, in preparation) that this structure can be modelled as a symmetrical relativistic outflow surrounded by modestly relativistic backflow.

The polarization image in Fig. 8(d) shows the extent of the region at the bright base of the main jet in which the magnetic field at the edges is parallel to the expanding outer isophotes, whereas the on-axis field is oblique (see also Fig. 8b). Finally, a 1.7-GHz MERLIN image of the main jet base (Fig. 8e) shows the position of the flaring point and the details of the initial expansion.

3.5 M 84

M 84 is of particular interest for two reasons: it has a much lower radio luminosity than the other sources we have studied and it shows very clear evidence for interaction with the surrounding IGM (Finoguenov et al. 2008).

Fig. 9(a) shows the total-intensity distribution over M 84 at 4.9 GHz with 1.65-arcsec FHWM resolution[6]. Both jets of this small (overall extent $\approx$12 kpc), low-luminosity radio source expand rapidly and deflect within about 1 arcmin. They are surrounded by diffuse emission (at least in projection) everywhere except perhaps within a few arcsec of the nucleus. The initially brighter N jet can be traced

[6] Lower-resolution (FWHM $\approx$4 arcsec) radio observations, shown by Laing & Bridle (1987), are not reproduced here.

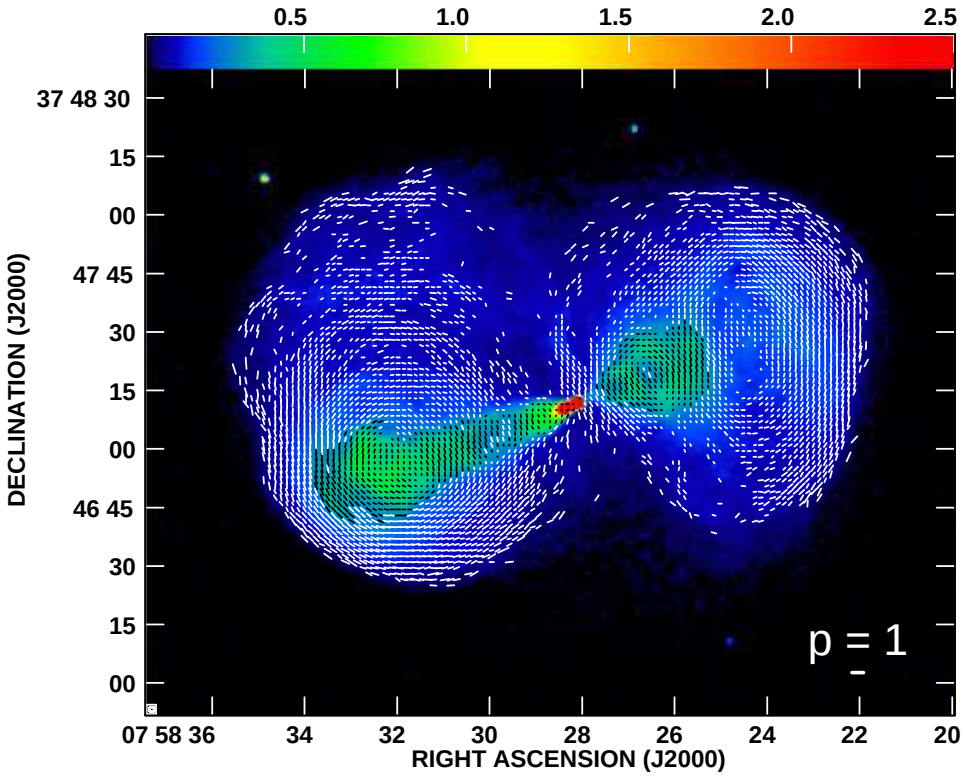

Figure 7. Vectors with lengths proportional to the degree of polarization at 4.9 GHz and directions along the apparent magnetic field, superimposed on a false-colour display of the total intensity over 0755+37 at 4.9 GHz. The resolution is 1.3 arcsec FWHM and the colour-scale range is 0 – 2.5 mJy beam^{-1}. The vector directions are derived from three-frequency RM fits at 4.0-arcsec resolution (Guidetti et al., in preparation).

as far as the edge of its lobe, where it bends through ≈90° in projection and decollimates on impact. The bending is accompanied by strong brightness gradients (Fig. 9b). In contrast, and uniquely amongst the sources in this paper, the S jet (initially fainter and misaligned with the nucleus) appears to terminate within its lobe and to feed a bubble-like structure with significant internal brightness gradients and filaments. The bubble is contained within a smoother, more elongated structure, at least in projection. The spectral index between 1.4 and 4.9 GHz (Fig. 9c) is constant with $\alpha \approx 0.6$ over the jets, within the Southern bubble and over most of the N lobe. The only regions of significantly steeper spectral index that we have detected (marked by arrows on Fig. 9c) are on both sides of the south jet base and to the west of the north jet. The current observations are too noisy to determine the spectral index in the low-surface-brightness emission outside the southern bubble. Fig. 9(d) shows the apparent magnetic field structure over the whole source at 1.65-arcsec FHWM resolution. The magnetic field in the S lobe is broadly circumferential and appears well-aligned with the peak in brightness gradient at the edge of the bubble. There is a sudden increase in the degree of polarization at the edge of the bubble, suggesting a discontinuity in the field structure at that location. A configuration in which the field is confined to ellipsoidal shells but is otherwise random (model A of Laing 1980) gives qualitatively the correct polarization distribution, but the predicted variation of p across the lobe is smoother than we observe. The magnetic field in the N lobe is predominantly perpendicular to the presumed path of the jet along its mid-line.

Fig. 10(a) shows the 4.9-GHz total-intensity distribution over the whole source at 0.4-arcsec FWHM resolution. This highlights the filamentary structure in the N lobe, the S bubble and a thin rim of emission around the S lobe. The intensity and gradient images of the jets at this resolution (Fig. 10b and c) emphasise the edges of both jets and the curved arcs in the north. The former also shows a curious thin feature (labelled A) joining the S jet and the edge of its lobe. The misalignment (non-collinearity) of the axes of the N and S jets beyond a few arcsec (a few hundred parsecs) from the nucleus and the initially knotty structure of the N jet, can be seen on a larger scale in Fig. 10(d), which also shows faint emission close to the nucleus on both sides.

Fig. 10(e) and (f) show that, although the apparent magnetic field in the jets is locally well-organised, there are significant regions where the field is oblique to the jet axis. In the outer parts of both jets the field appears to be predominantly perpendicular to the jet axis, but the jet emission also becomes blended with that from the lobes.

M 84 may be an intermediate case between lobed and tailed sources, showing some characteristics of each class. The N jet terminates in a sharp bend at the outer edge of its lobe, as often seen in lobed sources (eg. 3C 296, Section 3.6), but there are hints of a nascent tail structure in the NE. This is supported by *Chandra* imaging of M 84 (Finoguenov et al. 2008), which suggests that the NE lobe is breaking out of the surrounding hot plasma. In contrast, the S jet terminates well within its bubble-like lobe. The oscillation of the S jet prior to its eventual disruption is very reminiscent of that of the jets within the S spurs of the tailed sources 3C 31

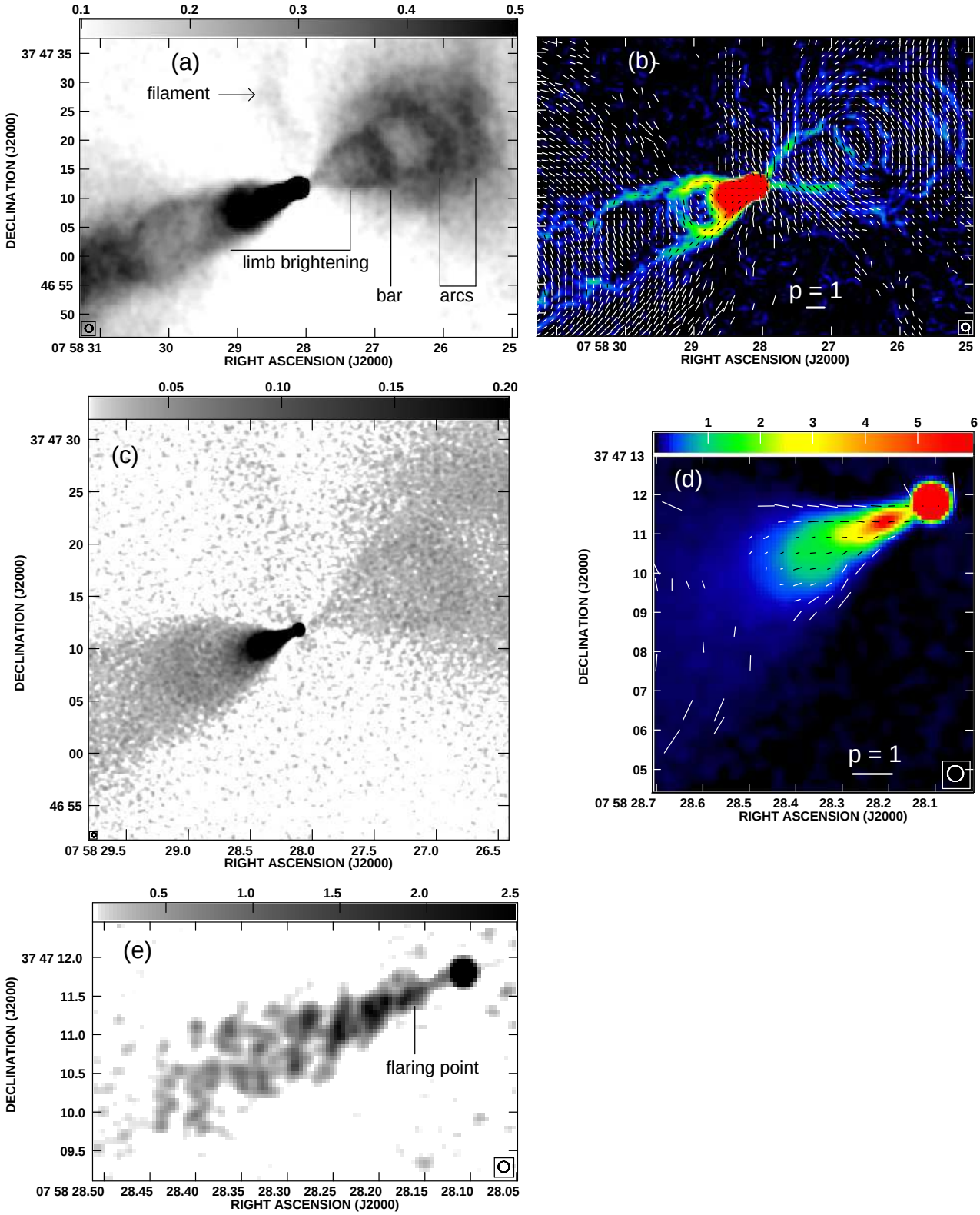

Figure 8. High-resolution images of the inner jets of 0755+37. (a) Total intensity at 4.9 GHz with 1.3-arcsec FWHM resolution, plotted with a compressed grey-scale range to emphasise fine-scale structure in and around the jets. (b) Vectors with lengths proportional to $p_{4.9}$ and directions along the apparent magnetic field superimposed on a false-colour image of intensity gradient at 4.9 GHz. The resolution is 1.3 arcsec FWHM. (c) Total intensity at 4.9 GHz, 0.4-arcsec FWHM. (d) Main jet base at 4.9 GHz with 0.4-arcsec FWHM resolution. $\mathbf{B}_{\rm a}$ vectors with lengths proportional to $p_{4.9}$ are superposed on a false-colour plot of total intensity. (e) MERLIN image of the main jet base at 1.7 GHz with 0.16-arcsec FWHM resolution (Bondi et al. 2000). Corrections for Faraday rotation in panels (b) and (d) were made using a three-frequency RM fit at 4.05-arcsec resolution (Guidetti et al., in preparation).

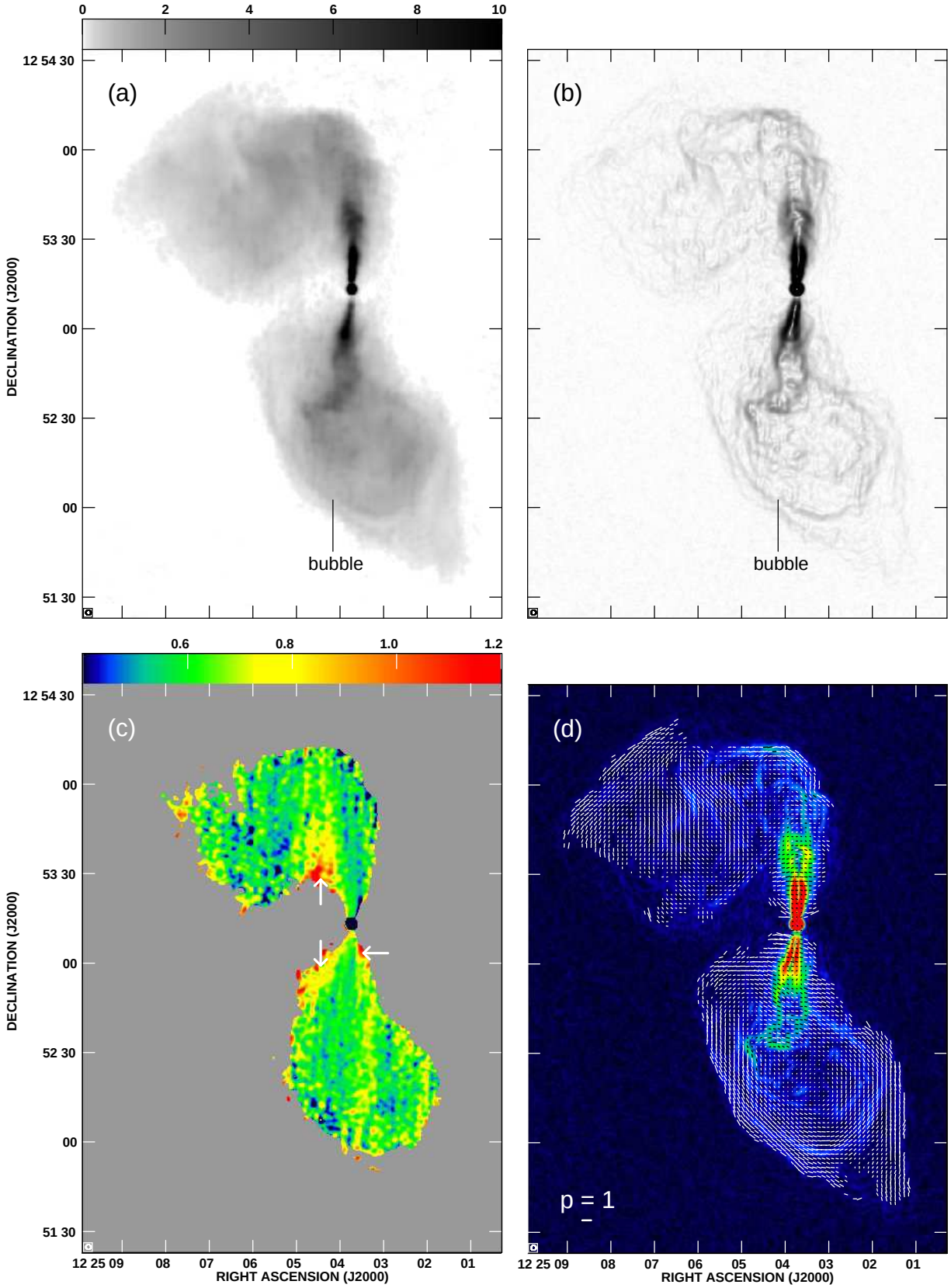

Figure 9. Images of M 84 at 1.65-arcsec FWHM resolution. (a) 4.9-GHz total intensity. (b) 4.9-GHz intensity gradient. (c) Spectral index between 1.4 and 4.9 GHz, plotted only where its rms error is <0.1. The vertical "streaks" are artefacts. Arrows mark the areas when the spectral index is significantly steeper than the typical value of $\alpha = 0.6$. (d) $\mathbf{B}_{\rm a}$ vectors with lengths proportional to $p_{4.9}$, superposed on a false-colour plot of intensity gradient. Corrections for Faraday rotation were made using a 4-frequency RM image at 4.5-arcsec resolution (Guidetti et al. 2011). All panels show identical areas.

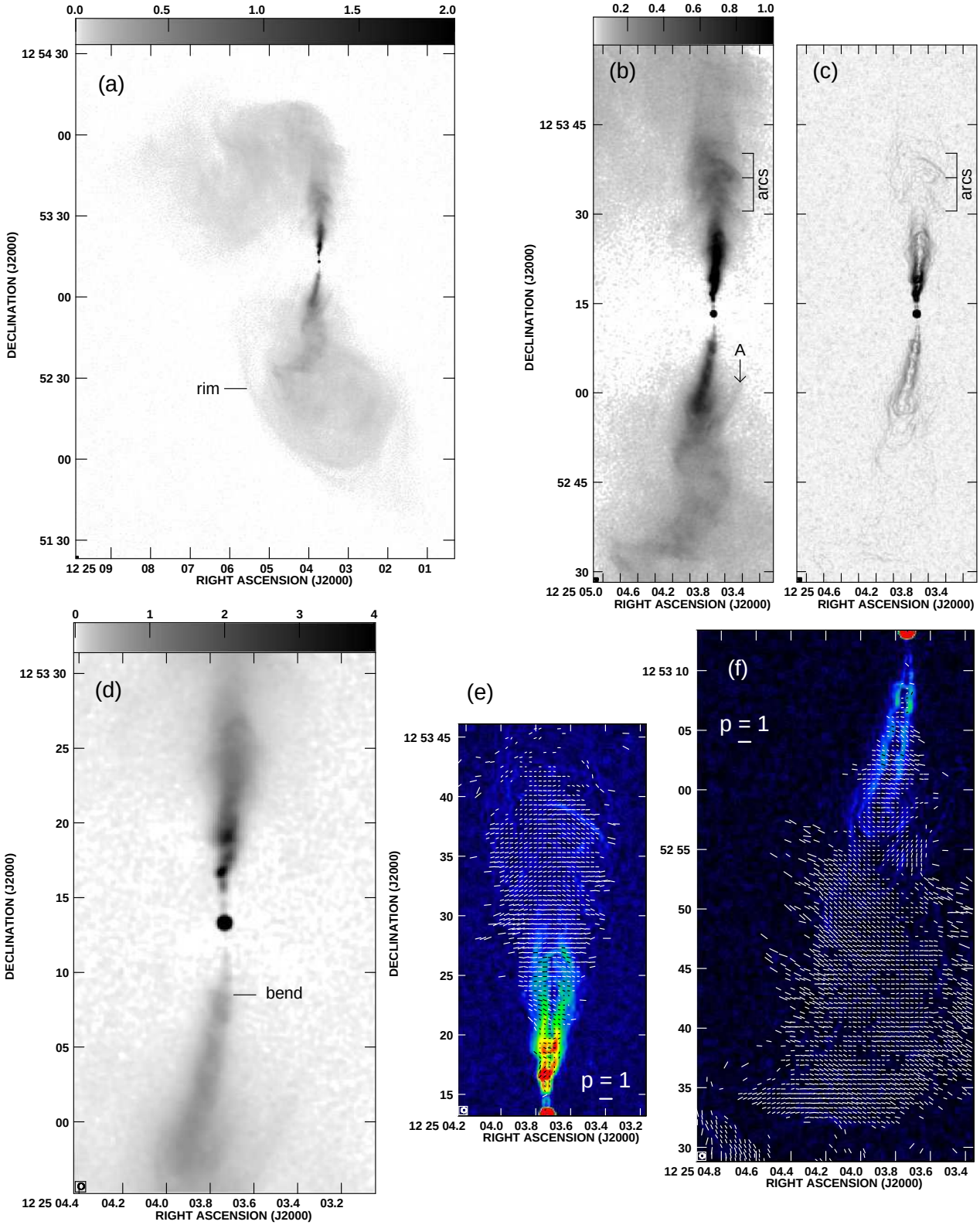

Figure 10. 4.9-GHz images of M 84 at 0.4-arcsec FWHM resolution. (a) Total intensity for the whole source. (b) Total intensity for the jets. (c) Intensity gradient for the jets. Three prominent "arcs" in the N jet are labelled on panels (b) and (c). (d) Total intensity for the inner jets, showing the abrupt bend in the counter-jet. (e) $\mathbf{B}_{\rm a}$ vectors with lengths proportional to $p_{4.9}$, superimposed on a false-colour image of intensity gradient for the N jet. (f) As (e), but for the S jet.

and 3C 449 (Laing et al. 2008; Katz-Stone & Rudnick 1997). The spectral gradients (such as they are) are more characteristic of lobed sources, with no hint of steepening outwards. The constancy of the spectral index across the radio structure is not surprising: given the small (≈12-kpc) size of the source, synchrotron losses are unlikely to have had enough time to steepen the spectrum at GHz frequencies even in the more extended regions.

3.6 3C 296

Fig. 11 shows the 1.4-GHz total intensity and brightness gradient together with the 1.4 to 4.9-GHz spectral index distributions over 3C 296 at 5.5-arcsec resolution. The intensity data are essentially those in Figs.1(a) and 4(a) of Laing et al. (2006b) with an improved deconvolution, but the grey-scale range in Fig. 11(a) is chosen to show the jets more clearly where they appear to enter the lobes. The corresponding intensity gradient is shown in Fig. 11(b). Lower limits to the spectral indices have been plotted outside the white intensity contour in Fig. 11(c) to provide a better representation of the large-scale spectral gradients at the edges of the radio source. There is clear evidence that the flatter-spectrum ($\alpha \approx 0.5$ to 0.65) jets propagate to the edges of both lobes, where they deflect and eventually blend with more extended steeper-spectrum emission whose spectral index $\alpha \approx 1$. The NE jet forms a cap of flat-spectrum emission with a semicircular outer boundary, again marked by sharp brightness gradients. The flow (as traced by its flatter spectrum) then turns through $\approx 140^\circ$ in projection, crosses the entire lobe and impacts on the boundary at the position marked on Fig. 11(b). The SW jet, on the other hand, does not form a cap, but appears to make an oblique impact on the wall of the lobe before turning through almost 180° in projection back towards the nucleus. The spectral index of the more extended emission increases further towards the centre of the source and towards its outer edges, where $\alpha \approx 2$.

3.7 0326+39

Fig. 12 shows the distributions of the 1.4-GHz total intensity and 1.4 to 4.9-GHz spectral index over 0326+39 at 18-arcsec FWHM resolution.

As in the other sources studied here, the lobes of 0326+39 appear to surround the jets in projection. Even at this relatively low resolution, the jets are clearly traceable to the outer parts of the lobes in both total intensity, where they appear to twist and deflect close to the outer edges of the lobes, and spectral index, where they can be traced as regions of significantly lower index. The W jet exhibits a particularly strong kink towards the S about 2 arcmin (≈ 60 kpc) from the nucleus; this kink is clearly replicated in the spectral index distribution.

The extended emission of both lobes also shows a well-defined spectral index gradient, increasing towards the nucleus from $\alpha \approx 1$ near the broad caps that appear to be dominated by the outer jet emission to a significantly steeper spectrum with $\alpha \approx 2$ near the centre of the source. The spectral index also appears to increase towards $\alpha \approx 2$ in the outer part of the faint Southward extension of the E lobe.

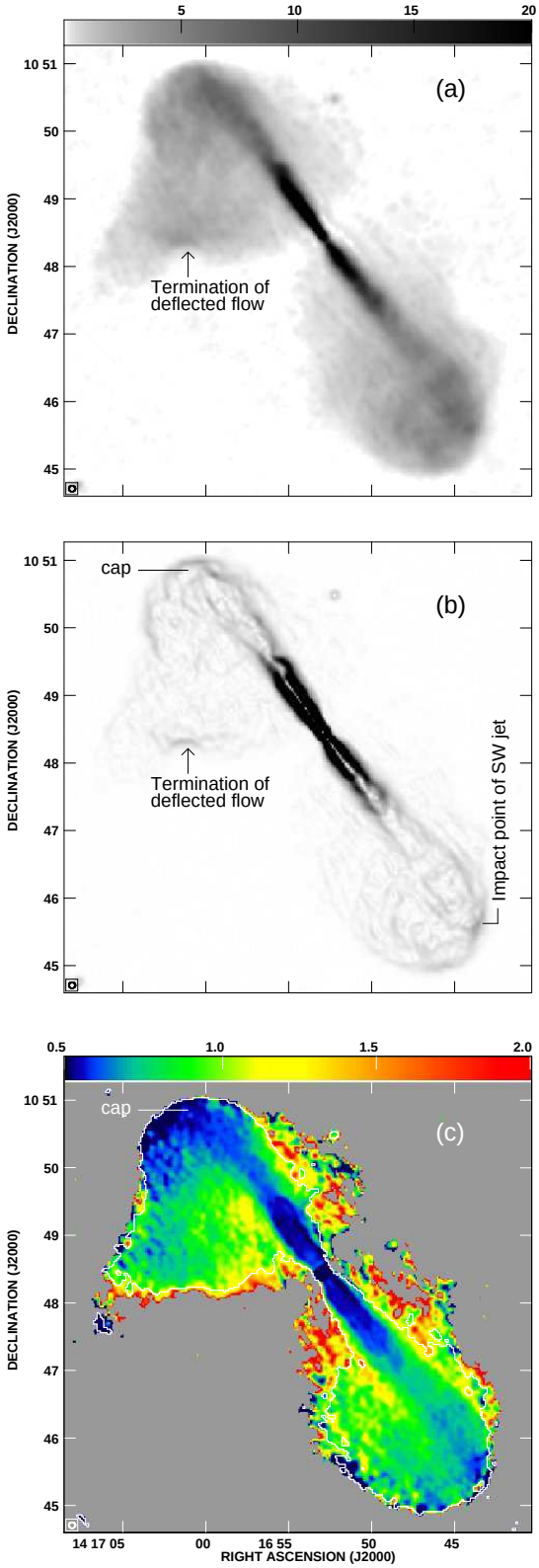

Figure 11. (a) Grey-scale of the 1.4-GHz total intensity over 3C 296 at 5.5-arcsec FWHM resolution. (b) Intensity gradient image at the same frequency and resolution as panel (a). (c) False-colour plot of the 1.4 to 4.9 GHz spectral index distribution at 5.5-arcsec FWHM resolution; data plotted outside the white contour are lower limits.

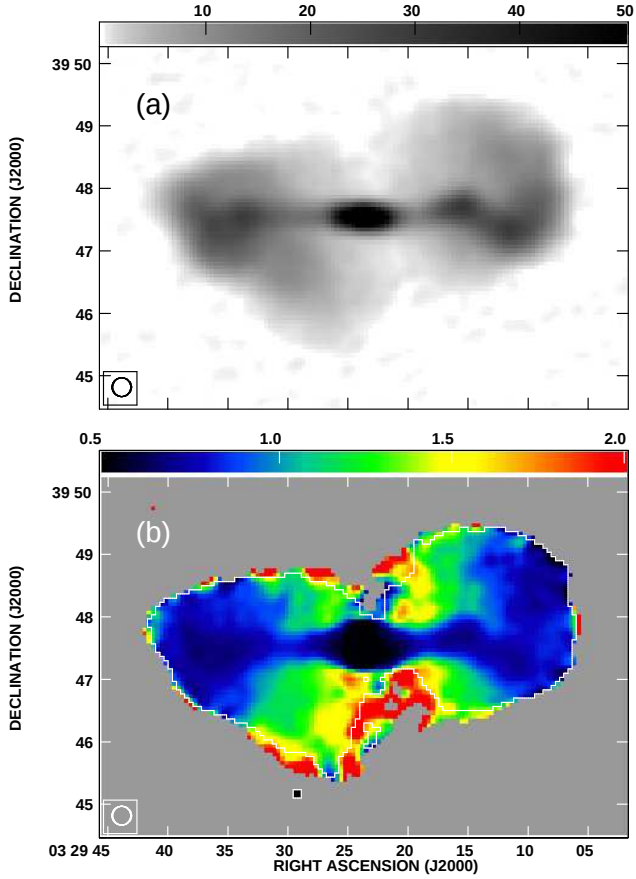

Figure 12. (a) Grey-scale of the 1.4-GHz total intensity over 0326+39 at 18-arcsec FWHM resolution. (b) False-colour plot of the spectral index ($\alpha_{1.4}^{4.9}$) distribution at the same resolution.

4 DISCUSSION

4.1 Initial jet propagation

There appear to be few, if any, morphological differences between the jet base regions in lobed and tailed FR I sources, whose common properties include the following.

(i) The initial rapid expansion (flaring) and recollimation of the jets is essentially identical in both types of FR I source.
(ii) Jet bases usually show significant side-to-side asymmetries, although a few very symmetrical examples of each type are known.
(iii) With the exception of these symmetrical cases, there are further common properties, as follows.

(a) One jet in each source exhibits a bright region at its base, often with with non-axisymmetric knots and a predominantly longitudinal magnetic field.
(b) Jet brightness and polarization asymmetries are correlated: the apparent magnetic field on-axis in the brighter jets is initially longitudinal, but switches to transverse at larger distances; that in the fainter jets is always transverse.
(c) The jet/counter-jet ratio falls with increasing distance from the nucleus.

These regions at the bases of FR I jets are also those in which our models (Laing & Bridle 2002a; Canvin & Laing 2004; Canvin et al. 2005; Laing et al. 2006b) show that the jets decelerate from relativistic to sub-relativistic velocities. The development of a *transverse* velocity gradient across the jets implies that they decelerate primarily by boundary-layer entrainment of the external medium. We suggest that this entrainment occurs primarily in the dense, kpc-scale coronae of hot plasma that surround the nuclei of twin-jet radio galaxies (probably with an additional contribution from stellar mass loss) and that the entrainment effectively turns off on large scales, as it must to avoid further decollimation. *Chandra* observations have revealed coronae of this type in 0206+35, 0755+37 (Worrall et al. 2001), 0326+39 (Hardcastle, private communication), M 84 (Finoguenov et al. 2008) and 3C 296 (Hardcastle et al. 2005; Croston et al. 2008); NGC 193 may have a similar component (Giacintucci et al. 2011). The coronae for which data are available have central electron densities of 10^5 to $7\times10^5\,\mathrm{m}^{-3}$, central pressures of 3×10^{-11} to $4\times10^{-10}\,\mathrm{Nm}^{-2}$ and core radii of 0.3 to 2 kpc. It seems likely that lobe plasma is excluded from the immediate vicinity of the nucleus by the high-pressure coronae, so the jets in both types of source initially propagate in essentially identical environments, unshielded from the IGM. Further evolution of the jets will depend on their surroundings: if they propagate through low-density lobe material, then entrainment will effectively cease and they will recollimate to become almost cylindrical flows, as seen in the sources described here. Entrainment rates are also likely to be small in jets without surrounding lobes provided that the external density is low. For example, there is no sign of any lobe surrounding the inner jets of NGC 315, yet it has a very small opening angle after recollimation (Canvin et al. 2005). This argues for a negligible entrainment rate at distances $\gtrsim 35$ kpc, and the external density does indeed fall rapidly on these scales (Croston et al. 2008). In contrast, we have argued that entrainment continues at a lower, but still significant rate after recollimation in 3C 31, whose inner jets also have no surrounding lobes. In this source, the opening angle after recollimation is larger, our models indicate continuing deceleration and there is a hot-gas component with a large core radius in addition to the inner corona (Laing & Bridle 2002b).

One feature of jet propagation appears to be unique to lobed sources, however. Our high-resolution data for 0206+35 and 0755+37 show that the apparent difference in opening angle between the main and counter-jets seen at lower resolution in these sources is a manifestation of a *two-component* jet structure. In both sources, the main jet and the counter-jet appear to contain both narrow (well-collimated) and broader features on both sides of the nucleus, but the better collimated parts of the main jet are centre-brightened while those in the counter-jet are centre-darkened. The broader features at the edges of the counter-jets are also slightly brighter than those of the main jets. What *appears* to be poorer collimation of the counter-jet at low resolution is now seen as a narrow centre-brightened jet opposite a similarly narrow centre-darkened counter-jet, surrounded by broader emission which is slightly brighter around the counter-jet than around the main jet. We will explore explanations for this "two-component" jet structure in terms of relativistic outflow in the well collimated component surrounded by mildly relativistic backflow in the

broader component in a later paper (Laing & Bridle, in preparation).

4.2 Jet termination and lobe structure

With the partial exception of M 84, to which we return at the end of this section, the sources described in this paper have lobes similar to those in FR II sources (e.g. Alexander and Leahy 1987; Carilli et al. 1991; Kharb et al. 2008). They exhibit sharp brightness gradients at their outer edges, spectral indices that steepen towards the nucleus from the outer lobes and towards the outer extremities of any lobe, off-axis wings of diffuse emission near their centres, and generally circumferential magnetic fields. The only obvious difference from the lobes of FR II sources is the evident lack of hot spots at the ends of the FR I jets. Similar spectral gradients occur in a larger sample of lobed FR I sources observed at lower resolution (Parma et al. 1999). Where the jets dominate the total intensity, they all have similar spectral indices in the range 0.5 to 0.7. Even when the jets are not obviously dominant in intensity alone, the observed spectral index distributions can trace plausible paths for jets towards the edges of the lobes. This spectral signature implies that steeper-spectrum lobe material has been displaced by flatter-spectrum jet material along an extended pathway through the lobes. Note that the spatial resolution of our data relative to the overall source size is higher than for most published multifrequency imaging of sources in either FR class. Together with the ability to trace the jet flow via its flatter spectrum and the use of intensity gradient images to indicate enhanced compression, our data allow us to identify a number of new types of structures in the lobes.

The jets often terminate in what we have called "caps", with the following properties.

(i) They typically occur at the ends of lobes (one example, 0755+37SE, appears recessed, perhaps as a result of projection) and are clearly associated with jet termination.
(ii) They are bounded at their leading edges by smooth outer isophotes (approximated by segments of circles) with sharp intensity gradients.
(iii) They also have inner boundaries, again marked by high intensity gradients.
(iv) Their emission has a flat spectrum, close to that typical of jets ($\alpha \approx 0.6$) after accounting for contamination by steeper-spectrum diffuse emission.
(v) Four out of five examples are fairly symmetrical with respect to the local jet axis. The exception is 3C 296NE.

There are five clear cases of such "caps" out of the ten FR I lobes we have studied at high resolution: NGC 193E and W, 0206+35NW, 0755+37SE and 3C 296NE, and 0755+37NW may well be similar.

Other jet terminations show some, but not all, of the same features. In particular, several show enhanced brightness gradients, but without obvious inner boundaries. In 0206+35SE, the jet bends away from its initial direction and creates a sharp brightness gradient where it impacts on the side of the lobe; the associated emission again has a relatively flat spectrum. Both lobes of 0326+39 probably have similar structures, but the available resolution is not yet high enough to be sure. In 3C 296SW and M 84N, the jets remain straight until they make oblique impacts on the lobe walls at locations marked by high intensity gradients after which they bend abruptly. The former case also shows flatter-spectrum emission at the impact point. 0755+37NW has a weak ring of emission surrounding a flatter-spectrum region, but this is contained entirely within the outline of the lobe. It is possible that some of these structures (especially the last) are caps seen from an unfavourable angle.

We see little convincing evidence for enhancements in $|\nabla I|$ *crossing* the jets close to their termination points, such as might be expected from strong shocks. This implies that the flow is internally sub- or transonic. Our estimates of the on-axis flow velocities after the initial rapid deceleration range from $\lesssim 0.1c$ to $\approx 0.6c$, compared with an internal sound speed of $3^{-1/2}c = 0.58c$ for an ultrarelativistic plasma. Unless there is significant deceleration on scales larger than we model, the implication is that the jets must be very light and energetically dominated by relativistic particles and magnetic field.

The lobes in this class of source are very different from the subsonic, buoyant plumes which are thought to form the outer structures of large FR I sources like 3C 31 (Laing et al. 2008). The picture that emerges for jet termination in lobed FR I sources is that the flow can be traced at least as far as the end of the lobe via its flatter spectrum. Where it impacts on the lobe surface, a high-pressure region (the cap) can be created. The smooth shape of the outer isophotes (compared with the more ragged outline of the lobes) suggests that the forward expansion is at least mildly supersonic with respect to the external medium. Jet material flows through the cap and back into the lobe, eventually mixing with pre-existing lobe plasma. The flow pattern is sometimes consistent with axisymmetry (or at least appears so in projection) but can bend by large angles without completely losing its collimation. The clearest example is 3C 296NE, where the flow bends by $\approx 140^\circ$ in the plane of the sky and can be traced as far as the trailing edge of the lobe, where its impact is marked by a sharp brightness gradient. An alternative to the formation of a cap appears to be an oblique collision with the boundary of the lobe. In at least one case, 0206+35SE, the jet deflects from its original straight path before hitting the edge of the lobe. This raises the possibility that the impact point moves around the surface of the lobe, extending it in different directions at different times and lowering the average advance speed of the lobe compared with the instantaneous speed of the impact point, as in the "dentist's drill" model of FR II sources (Scheuer 1982).

As noted in Section 3.5, M 84 appears to be an intermediate case, in which only one of the jets appears to impact on its lobe boundary, but no tails have (yet) developed. The S lobe of M 84 is morphologically very similar to the spurs in 3C 31, albeit on a much smaller linear scale. This adds to the developing picture of the transition between fast, well-collimated jets and slow plumes in tailed FR I sources, which is often a two-stage process. The jets first enter bubbles, within which they disrupt, often thrashing around (as in M 84S) before disintegrating completely. The tails are then formed by escape of material from the bubbles along the direction of steepest pressure gradient rather than directly from the jet flow. A similar morphology is often found in wide-angle tail sources (Hardcastle & Sakelliou 2004).

5 SUMMARY

We have presented deep, high-resolution, multi-configuration VLA imaging of four FR I radio sources: NGC 193, 0206+35, 0755+37 and M 84, together with lower-resolution observations of 0326+39 and a reanalysis of our published images of 3C 296. These sources are all examples of "lobed" FR I radio galaxies. Our results, displayed as images of total intensity, brightness gradient, degree of polarization, apparent magnetic-field direction and spectral index, show common features, as follows.

(i) All of the sources have twin radio jets, with side-to-side brightness ratios decreasing with distance from the nucleus in a manner qualitatively consistent with relativistic, decelerating flow.

(ii) The brightness and polarization distributions of the inner jets are very like those in tailed radio sources, indicating similar deceleration physics. We suggest that the jets in both classes of source propagate unshielded from the surrounding IGM within dense, kpc-scale coronae, leading to efficient boundary-layer entrainment.

(iii) Farther from the nucleus, the jets in both classes of source recollimate. This implies that the entrainment rate is low whether or not they are surrounded by lobe plasma.

(iv) 0206+35 and 0755+37 show evidence for a two-component jet structure in which a centre-brightened main jet and centre-darkened counter-jet are surrounded by broader features that are somewhat brighter on the counter-jet side, suggesting that a central relativistic outflow is surrounded by a slower, but still mildly relativistic backflow.

(v) In all but one case (M 84S), the jets propagate to the ends of their lobes. Continuing, but less well collimated flow can often be traced in spectral index or brightness gradient images.

(vi) Five or six of the ten jets we have studied at high resolution terminate at the ends of their lobes in features we call "caps" with smooth outer isophotes, sharp inner and outer intensity gradients and relatively flat spectra.

(vii) An additional three out of ten jet terminations are best described as oblique collisions of jets with the outer lobe walls: they also show enhanced outer intensity gradients and flat spectra and may be caps seen at unfavourable angles.

(viii) The lobes resemble those in FR II sources, with sharp outer brightness gradients, spectral indices which steepen towards the nucleus and circumferential apparent magnetic fields.

(ix) There is little evidence for features in the jet brightness distributions which can be identified as strong shocks, either at recollimation or where they terminate[7]. This implies that the flow is internally sub- or trans-sonic on large scales.

We will present quantitative modelling of the inner jets in later papers.

ACKNOWLEDGEMENTS

We thank Anita Richards for a useful perl script.

[7] Shocks may occur on smaller scales, at or just downstream of the flaring point.

REFERENCES

Alexander P., Leahy J.P., 1987, MNRAS, 225, 1
Baars J.W.M., Genzel R., Pauliny-Toth I.I.K., Witzel, A., 1977, A&A, 61, 99
Becker R.H., White R.L., Edwards A.L., 1991, ApJS, 75, 1
Bondi M., Parma P., de Ruiter H., Fanti R., Laing R.A., Fomalont E.B., 2000, MNRAS, 314, 11
Bridle A., Baum S., Formalont E., Fanti R., Parma P., Ekers R., 1991, A&A, 245, 371
Canvin J.R., Laing R.A., 2004, MNRAS, 350, 1342
Canvin J.R., Laing R.A., Bridle A.H., Cotton W.D., 2005, MNRAS, 363, 1223
Carilli C.L., Perley R.A., Dreher J.W., Leahy J.P.,1991, ApJ, 383, 554
Cheung C.C., 2007, AJ, 133, 2097
Cornwell T.J., Evans K.F., 1985, A&A, 143, 77
Croston J.H., Hardcastle M.J., Birkinshaw M., Worrall D.M., Laing R.A., 2008, MNRAS, 386, 1709
Falco E.E., et al., 1999, PASP, 111, 438
Fanaroff B.L., Riley J.M., 1974, MNRAS, 167, 31P
Finoguenov A., Ruszkowski M., Jones C., Brüggen M., Vikhlinin A., Mandel E., 2008, ApJ, 686, 911
Giacintucci S., et al., 2011, ApJ, 732, 95
Gregory P.C., Condon J.J., 1991, ApJS, 75, 1011
Greisen E.W., Spekkens K., van Moorsel G.A., 2009, AJ, 137, 4718
Griffith M.R., Wright A.E., Burke B.F., Ekers R.D., 1995, ApJS, 97, 347
Guidetti D., Laing R.A., Bridle A.H., Parma P., Gregorini L., 2011, MNRAS, 413, 2525
Hardcastle M.J., Sakelliou I., 2004, MNRAS, 349, 560
Hardcastle M.J., Worrall D.M., Birkinshaw M., Laing R.A., Bridle A.H., 2005, MNRAS, 358, 843
Katz-Stone D.M., Rudnick L., 1997, ApJ, 488, 146
Kharb P., O'Dea C.P., Baum S.A., Daly R.A., Mory M.P., Donahue M., Guerra E.J., 2008, ApJS, 174, 74
Kühr H., Witzel A., Pauliny-Toth I.I.K., Nauber U., 1981, A&AS, 45, 367
Laing R.A., 1980, MNRAS, 193, 439
Laing R.A., Bridle A.H., 1987, MNRAS, 228, 557
Laing R.A., Bridle A.H., 2002a, MNRAS, 336, 328
Laing R.A., Bridle A.H., 2002b, MNRAS, 336, 1161
Laing R.A., Peacock J.A., 1980, MNRAS, 190, 903
Laing R.A., Parma P., de Ruiter H.R., Fanti R., 1999, MNRAS, 306, 513
Laing R.A., Canvin J.R., Cotton W.D., Bridle A.H., 2006a, MNRAS, 368, 48
Laing R.A., Canvin J.R, Bridle A.H., Hardcastle, M.J., 2006b, MNRAS, 372, 510
Laing R.A., Bridle A.H., Parma P., Feretti L., Giovannini G., Murgia M., Perley R.A., 2008, MNRAS, 386, 657
Leahy J.P., Perley R.A., 1991, AJ, 102, 537
Miller N.A., Ledlow M.J., Owen F.N., Hill J.M., 2002, AJ, 123, 3018
Morganti R., Fanti C., Fanti R., Parma P., de Ruiter H.R., 1987, A&A, 183, 203
Ogando R.L.C., Maia M.A.G., Pellegrini P.S., da Costa L.N., 2008, AJ, 135, 2424
Parma P., de Ruiter H.R., Fanti R., 1996, in Extragalactic Radio Sources, eds Ekers R.D., Fanti C., Padrielli L., IAU Symp. 175, Kluwer, Dordrecht, p. 137

Parma P., Murgia M., Morganti R., Capetti A., de Ruiter H.R., Fanti R., 1999, A&A, 344, 7
Scheuer P.A.G., 1982 in Extragalactic Radio Sources, eds Wade C.M., Heeschen D.S., IAU Symp. 97, Kluwer, Dordrecht, p. 163
Simard-Normandin M., Kronberg P.P., Button S., 1981, ApJS, 45, 97
Sobel I., Feldman G., 1968, unpublished, http://en.wikipedia.org/wiki/Sobel_operator
Trager S.C., Faber S.M., Worthey G., Gonzalez J.J., 2000, AJ, 119, 1645
Ulvestad J.S., Perley R.A., Chandler C.J. 2009, The Very Large Array Observational Status Summary, NRAO, Socorro, http://www.vla.nrao.edu/astro/guides/vlas/current/
Young A., Rudnick L., Katz D., Delaney T., Kassim N.E., Makishima K., 2005, ApJ, 626, 748
VLA Staff, 2010, EVLA Transition for Observers, http://www.vla.nrao.edu/astro/guides/evlareturn/vla-evla/
Wardle J.F.C., Kronberg P.P., 1974, ApJ, 194, 249
White R.L., Becker R.H., 1992, ApJS, 79, 331
Worrall D.M., Birkinshaw, M., Hardcastle M.J., 2001, MNRAS, 326, L7
Wright A., Otrupcek R., 1990, Parkes Catalogue 1990, Australia Telescope National Facility